

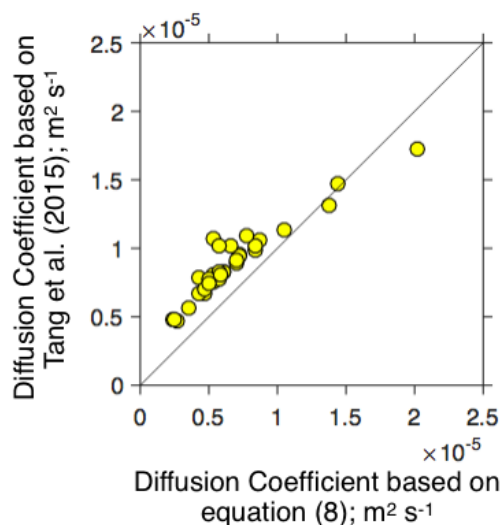
We thank both reviewers for their comments. We have revised the manuscript based on their comments and queries and provided a point-by-point response below. Reviewer comments are in regular black, our response is in blue, and the additions/updated text from the manuscript are in red.

Reviewer 1

1. Pg. 4 Ln. 149: Somewhere in Sect. 2.1, can you state the OFR residence time used in these experiments? It must be given in Jathar 2017a, but it would be useful to quote it here directly for context when you discuss specific condensational sink lifetimes below.

The OFR residence time used in Jathar et al. (2017) was 100 seconds. We have mentioned the residence time in the revised text: “The OFR had a residence time of 100 s.”.

2. Pg. 7 Ln. 271: How well does this method of estimation of the diffusion coefficient work? Can you provide any references where this method has been tested and used before? If not, please state your reasoning for using it, or better yet include a simple figure comparing the values of D estimated using this equation with independent measurements/calculations of D for several typical species, to illustrate that it works well enough. (It might also be the case that your results are insensitive to variations in D).



The method to estimate the gas-phase diffusion coefficient was previously used by Zhang et al. (2014) to model SOA formation from toluene photo-oxidation using the statistical oxidation model (SOM). We have added the Zhang et al. (2014) reference before we introduce the equation in the revised text. The diffusion coefficients calculated using equation 7 in the text were evaluated against diffusion coefficients compiled by Tang et al. (2015) for a suite of organic compounds. The comparison is shown in the figure to the side. The equation used in this work under-predicted the diffusion coefficient by ~30% for species with a value lower than $10^{-5} \text{ m}^2 \text{ s}^{-1}$. We examined the sensitivity in the model predictions to the use of a higher diffusion coefficient. Increasing the diffusion coefficient by a factor of two did not have any impact

on the model predictions of OA for the Idle-Diesel-None experiment performed on June 5. The following text was added to the methods section after describing the equations for calculating the gas-phase diffusion coefficient: “This formulation to calculate the gas-phase diffusion coefficient under-predicted the measured gas-phase diffusion coefficients compiled by Tang et al. (2015) by ~20%. However, doubling the gas-phase diffusion coefficient calculated in equation 8 resulted in very small change (<1%) in the OA mass predictions for a representative experiment. Hence, we decided to use the formulation in equation (8) for the rest of the work.”

3. Pg. 10 Ln. 357: Your numbers 1 through 3 here are mostly repeating information you have already given the reader in the prior sections (number 4 is mostly new text). It’s OK to leave this

text if you want to summarize and emphasize the paper organization, but you could consolidate/remove the duplicate text to streamline your Methods section.

We agree with the reviewer that the sections preceding section 2.5 already describe the various simulations performed in this work. However, section 2.5 provides an overview of all the simulations for the reader to review/jump back to when reading through the results.

4. Pg. 18 Ln. 691-696: I think it would really enhance this section if you could expand upon your discussion of Fig. 8 and related text. For instance, you've calculated for a 100s residence time, but what does it look like for the residence times of 2-4 min that have been used in most of the ambient studies, e.g. Palm et al. 2016 that you cite previously? How does this compare to the discussion in Sect. 3.3 of Palm et al. 2016, which is similar to the analysis presented here? They have suggested that the use of seed aerosol (to increase condensational sink) and the use of longer residence times could avoid such issues; can you use your results to provide support for such conclusions, or better yet provide quantitative guidance for future OFR studies (e.g. use residence times greater than X min or a minimum seed surface area)? Such suggestions would provide a great reference for the growing OFR user community.

Based on the reviewer's suggestion, we performed simulations with an OFR residence time of 2 and 4 mins for both the 10 and 100 nm initial particle sizes. In our original text, we had commented on the influence of the initial condensational sink. We found that the initial condensational sink had to be very large ($>5 \text{ min}^{-1}$) to produce the same SOA as that under instantaneous partitioning conditions and hence would be very hard to achieve in ambient applications of the OFR. If the initial condensational sink were smaller, the use of a smaller particle size distribution could help but would still be insufficient in ambient applications of the OFR. In the revised text, simulations with the two different residence times suggested that the residence times did not have a significant impact on our conclusions. Based on the simulation results, we recommend that the OFR be operated with very high initial condensational sinks ($>1 \text{ min}^{-1}$) in case the SOA formed is less than $100 \mu\text{g m}^{-3}$. If larger amounts of SOA are expected to be formed, it might be possible to operate the OFR with lower initial condensational sinks. We also state that these results will need to be experimentally verified. We have expanded on the original text as follows: "To explore the relative importance of instantaneous and kinetically-limited partitioning in an OFR, we used the SOM to simulate SOA formation from diluted diesel exhaust using instantaneous and kinetic partitioning assumptions for varying amounts of SOA formed ($1\text{-}10000 \mu\text{g m}^{-3}$) and initial condensational sinks ($0.001\text{-}10 \text{ min}^{-1}$). These simulations were similar to the calculations performed by Palm et al. (2017) where they calculated timescales and losses of condensable SOA vapors to the OFR walls and sampling lines and reaction with OH. The calculations were performed for two different initial particle sizes (10 and 100 nm) since the condensation of SOA mass would grow the initial condensational sink for the two particles at different rates, i.e. for the same starting initial condensational sink, smaller particles would experience quicker growth in the condensational sink compared to larger particles for the same amount of condensing mass. The calculations were also performed for two different residence times – 2 and 4 minutes – to span the residence time range used in typical applications of the OFR. We assumed an accommodation coefficient of 0.1. The results plotted in Figure 8 show the ratio of SOA predicted through kinetic partitioning to that predicted through instantaneous partitioning as a function of the initial condensational sink and the SOA formed under an instantaneous partitioning assumption. Across the four scenarios explored (two initial particle sizes and two residence times), the SOA formation predicted under the kinetic

partitioning assumption was an order of magnitude or more lower than that predicted under the instantaneous partitioning assumption over a large portion of the input range explored, e.g., when the initial condensational sink was smaller than $\sim 0.1 \text{ min}^{-1}$ and the maximum SOA formed was lower than $\sim 100 \mu\text{g m}^{-3}$ for the 10 nm simulations and lower than $\sim 1000 \mu\text{g m}^{-3}$ for the 100 nm simulations. We also found that the SOA formation in the OFR was kinetically-limited under typical ambient conditions. The SOA formation predicted under the kinetic partitioning assumption approached the SOA formed under the instantaneous partitioning assumption either when the initial condensational sink was very large ($> 5 \text{ min}^{-1}$) or when a large amount of condensable SOA was produced in the OFR ($\geq 1000 \mu\text{g m}^{-3}$ for the 10 nm particles and $\gg 10000 \mu\text{g m}^{-3}$ for the 100 nm particles). Our finding implies that ambient applications of the OFR, where initial condensational sinks are typically smaller ($\sim 0.005\text{-}0.5 \text{ min}^{-1}$) and the maximum SOA produced is typically less than $40 \mu\text{g m}^{-3}$, will only produce a small fraction (0-30%) of the intended SOA. Furthermore, our simulations suggested that a smaller initial particle size (i.e., 10 nm) for the same initial condensational sink and a longer OFR residence time (i.e., 4 min) may not necessarily help produce the intended SOA under ambient conditions. Although these simulation results need to be verified experimentally, they do suggest that it might be challenging to operate the OFR in conditions where instantaneous or atmospherically-relevant partitioning is applicable, further complicating the coupled atmospheric simulation of chemistry and thermodynamics in OFRs.”.

Technical Comments:

Pg. 5 Ln. 168: Please define ‘THC’.

This has been corrected.

Table 1: Are some/all of the values reported in this table already reported in the Jathar et al 2017a reference, or are they new data presented in this work? If the former, you should cite that paper in the table caption.

All values in Table 1, except for the information on the particle size distribution, have been reported in Jathar et al. (2017a). We have added the citation to the figure caption.

Pg. 5 Ln. 192: It’s confusing that you’re using ‘VOC’ to represent all of the organic gases including SVOCs and IVOCs. I suggest you refer to them as ‘organic gases’ instead of ‘VOCs’ in such instances, so you keep the nomenclature clean.

We have revised the text in the entire manuscript to refer to VOCs, SVOCs, and IVOCs together as organic precursors.

Fig. 1c: Please label the yellow pie slices in the VBS and SOM pies.

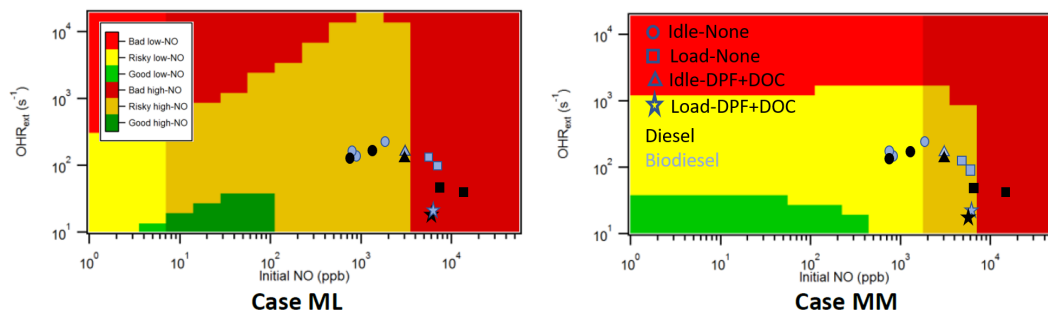
We apologize for the omissions. The yellow pie refers to the SOA formed from alkanes. The label has been added to Figure 1(c).

Reviewer 2

1. Peng and Jimenez (2017) have published a characterization of whether the chemistry in OFRs with high initial NO is similar or very different from that in the atmosphere. The results on Figure 4 of that paper can be used to approximately determine whether the cases studied here fall

in the good / risky /bad regions and whether the chemistry is predominantly in a low or high NO regime. This is important information that should be included in the paper.

We thank the reviewer for this important comment. Based on the information in Table 2, the experiments of Jathar et al. (2017a) were most appropriately represented by the ML and MM cases although some of the experiments were beyond the MM case. The figure below shows the data from this work overlaid on Figure 4 from Peng and Jimenez (2017). This comparison suggested that we use the high NO_x parameterizations to model SOA formation for most of the experiments in this work.



To improve our precision, we contacted Zhe Peng (first author of the Peng and Jimenez (2007) paper) and Zhe helped us run their model to determine low versus high NO conditions for all our experiments. For each experiment, the model was run with initial values of the external OH reactivity contributed by CO and THC, NO and NO₂ concentrations, the photon flux at each photochemical exposure, and the relative humidity. Model results suggested that the OFR ran in a high NO mode at all photochemical exposures when the engine was run at load conditions or with an aftertreatment device in place. However, the model predicted that the OFR ran in a low NO mode at most of the photochemical exposures when the engine was run at idle conditions and without an aftertreatment device (i.e., Idle-Diesel-None and Idle-Biodiesel-None). These findings from the Peng and Jimenez (2017) model were used to inform the choice between low and high NO_x parameterizations to model SOA formation. The following text was added to Section 2.1 to briefly describe the problem and results from the Peng and Jimenez (2017) model:

“Although the diesel exhaust was diluted with clean air to produce atmospherically-relevant concentrations of POA, the initial THC, CO, and NO_x concentrations in the OFR were still quite high. Peng and Jimenez (2017) using a detailed gas-phase model argued that the high external OH reactivity might lead to non-OH chemistry in the OFR and NO could quickly be consumed in the OFR leading to low NO conditions for SOA formation. Peng and Jimenez (2017) quantified the potential influence of NO on the oxidation chemistry by calculating the ratio of the reactive flux of the peroxy radicals with NO to the reactive flux of the peroxy radicals with HO₂ ($r_{\text{RO}_2+\text{HO}_2}/r_{\text{RO}_2+\text{NO}}$). A ratio greater than 1 was considered as “high NO” while a ratio less than 1 was considered “low NO”. For the relative humidity, photon flux, initial NO, and external OH reactivity values in Jathar et al. (2017a), the model of Peng and Jimenez (2017) predicted that the OFR ran in a high NO mode at all photochemical exposures when the engine was run at load conditions or with an aftertreatment device in place. However, the model predicted that the OFR ran in a low NO mode especially at the high photochemical exposures when the engine was run at idle conditions and without an aftertreatment device (i.e., Idle-Diesel-None and Idle-Biodiesel-None). The $r_{\text{RO}_2+\text{HO}_2}/r_{\text{RO}_2+\text{NO}}$ ratio and low versus high NO mode for each experiment and

photochemical exposure is listed in Table S1. Based on these results, we accordingly used the low and high NO_x parameterizations to perform the model simulations.”.

The low NO_x SOA parameterizations for the VBS and SOM models were included in Tables 3 and 5 respectively. All figures and the corresponding discussion in the results section were revised based on the use of the new parameterizations. For the full set of changes, please refer to the marked Word document included along with the response.

2. High-NO_x parametrizations were used in this study, while Peng and Jimenez (2017) found that high-NO_x conditions are very unlikely to be realized in OFR by initial NO injection only. (This can be verified with the previous suggestion) Low-NO_x SOA yields are often significantly higher than high-NO_x ones and SOA formed under low-NO_x conditions tends to have higher O:C (the results on elemental ratio in this study might be an evidence for this). The paper acknowledges that OA is 65% higher in a sensitivity test when low-NO_x yields were used. The validity of the modeling in this study is thus questionable, and the agreement in e.g. Figure 1 appears to be for the wrong reasons. The authors should show their simulation results for experiments using low- NO_x parametrizations and correct their conclusions if needed.

As mentioned in the previous comment, we used the Peng and Jimenez (2017) model to determine if we needed the low versus high NO_x parameterization to model the SOA formation across the experimental matrix and at different photochemical exposures. The Peng and Jimenez (2017) model recommended the use of low NO_x parameterizations for the Idle-Diesel/Biodiesel-None experiments and the use of high NO_x parameterizations for all the remaining experiments. The use of an experiment/photochemical exposure-specific SOA parameterization resulted in three key changes to the manuscript. First, this resulted in a modest change in the IVOC fraction that allowed for the most optimum model-measurement comparison across the entire experimental matrix: 30% in the revised work versus 40% in the original work. Second, it resulted in a better O:C comparison at the optimum IVOC fraction compared to the original work and produced slight differences in the SOM versus CIMS comparison performed in Figure 6. Third, the use of a low NO_x parameterization to model SOA resulted in a substantial increase in the SOA formed in the Idle-Diesel-None experiment, which was used as the representative experiment to discuss results in Figures 1, 2, 3, 5, 6, and 7. To keep the discussion in these figures centered around understanding the influence of the chemistry, thermodynamic, or OFR process, we updated the IVOC fraction used in the base case to ensure a good model-measurement comparison for this particular experiment. A lot of small changes have been made in the manuscript to reflect this update so please refer to the marked Word document included along with the response.

3. Line 209 and elsewhere: Ahlberg et al. (2017) did systematic experiments and VBS modeling to show that SOA growth in OFR is kinetically limited at low OA mass loading. This paper also needs to be cited for discussions on the kinetic limitation of SOA growth.

We thank the reviewer for pointing this out. We have folded the Ahlberg et al. (2017) study and cited it along with Lambe et al. (2015), Palm et al. (2016), and Jathar et al. (2017a).

4. Line 292: The POA VBS has more bins than the SOA ones shown in Table 2. How are the extra POA bins treated? Do they participate in aging?

The VBS in our numerical model is initialized with C^* bins ranging for 10^{-2} to $10^6 \mu\text{g m}^{-3}$ to ensure we accommodate the full range of POA volatilities. For first-generation SOA, the C^* bins other than those listed in Table 2 and 3 are zeroed out. Multigenerational aging for both POA and SOA is modeled using the scheme of Robinson et al. (2007) where mass in each C^* bin is allowed to react with OH and yield a product with a C^* that is an order of magnitude lower than the direct precursor, to a lower limit C^* of $10^{-2} \mu\text{g m}^{-3}$.

5. Line 360: The reason why $\alpha=0.1$ is assumed is not clear to me until I arrive at the end of Section 3.2. A brief explanation or a reference to Section 3.2 is needed.

We have added a note here referring to the relevant sections: “The choices for the base case are discussed in Sections 3.2 and 3.3.”.

6. Line 386: Why do curves in Panels a and b of Figure 1 look slightly different? E.g. the measurement point at highest age is located between the VBS and SOM predictions in Figure 1a while it overlaps with the VBS one in Figure 1b.

Thank you for pointing that out. The measurements in Figure 1(b) were not being calculated correctly. This has been corrected.

7. Line 388: Why does an overprediction of x_3 occur at low ages? This should be discussed further.

The over-prediction in Figure 1 that simulates the OA evolution using the base case is mostly a result of choosing a 30% IVOC fraction. The 30% IVOC fraction was chosen for the base case to produce the best global model-measurement comparison across all photochemical exposures and all experiments. The model-measurement comparison, visualized in Figure 4(c) (top panel), exhibits a fractional bias of 6% suggesting that the use of a 30% IVOC fraction did not over- or under-predict the OA mass with photochemical exposure. It just so happens that the 30% IVOC fraction for the Idle-Diesel-None experiment over-predicted the OA mass at lower photochemical exposures but produced a reasonable comparison at higher photochemical exposures. In contrast, the use of the 30% IVOC fraction resulted in the opposite effect for the Idle-Diesel-DPF+DOC experiment shown in Figure 2(b) where the base case model (dashed lines) produced reasonable agreement at the lower photochemical exposures but under-predicted the OA mass at higher photochemical exposures. We have added the following text to address this comment: “Our base case seemed to offer a mixed model-measurement comparison for this specific experiment (i.e., over-prediction at lower photochemical ages and a slight under-prediction at higher photochemical ages) because the 30% IVOC mass fraction used in the base case was optimized to achieve a favorable model-measurement comparison across all experiments at all photochemical exposures. In other words, the over-prediction in this experiment at lower photochemical exposures was probably offset by an under-prediction at similar photochemical exposures for some of the other experiments. It is important to note that the model performance varied across the suite of experiments and this overall model performance is discussed in more detail in Section 3.3.”.

8. Line 431: Palm et al. (2016) reported that a low value of the accommodation coefficient ($\ll 1$) was inconsistent with their ambient OFR SOA formation experiments. A more direct measurement of the accommodation coefficient of SOA (compared to the more indirect measurements on the publications cited here) has been recently published by Krechmer et al.

(2017), with measured values in the range 0.5-1. Both of these results support the use of higher values for accommodation coefficient and thus support the conclusions here.

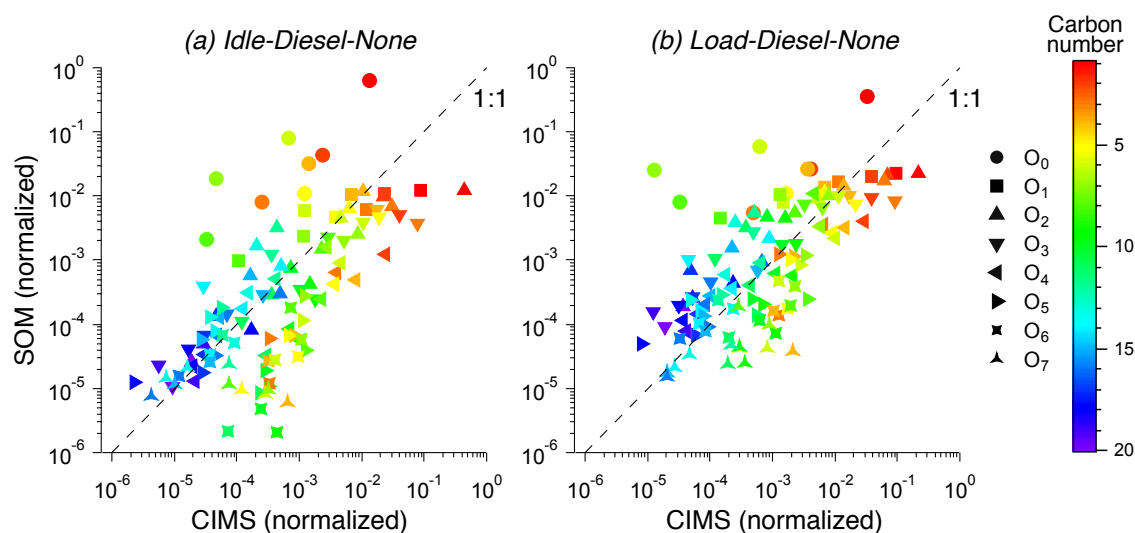
The studies of Palm et al. (2016) and Krechmer et al. (2017) are cited as part of the mass accommodation discussion: “This α value for diesel exhaust SOA was consistent with prior estimates of the α value for biogenic SOA estimated from chamber, OFR, and aerosol heating experiments (Lee et al., 2011; Saleh et al., 2013; Karnezi et al., 2014; Palm et al., 2016) and direct measurements of α for alkanol SOA (Krechmer et al., 2017). However, an α of 0.1 was an order of magnitude higher than that observed recently for toluene SOA under dry conditions (Zhang et al., 2014). Model results presented hereafter include a kinetic treatment of gas/particle partitioning and assumed an accommodation coefficient of 0.1.”

9. Line 443: In Figure 3b, Curves (iv) appear to be higher than Curves (ii). However, the condensational sink of (ii) is always that at the end of the growth while that of (iv) starts from 1 nm particles (identical number concentration). The average of the latter is obviously lower than that of the former and hence less OA will condense in the case of (iv) in theory. Why does Figure 3b show the opposite?

The OA mass predictions for curves (ii), (iii), and (iv) are quite similar and the small differences between them can be attributed to the coupled interaction of multi-generational aging and kinetic gas/particle partitioning. The following text has been added: “Slight differences between the different curves for the Idle-Diesel-None experiment and curves (ii), (iii), and (iv) for the Idle-Diesel-DPF+DOC experiment can be attributed to the interaction of multigenerational aging and kinetic gas/particle partitioning.”

10. Line 564: Figure 6 is supposed to convey important information. But it is impossible for me to tell data points for similar carbon numbers, so that I cannot verify relevant claims made in Sections 3.4. I suggest using different markers/patterns instead of point size to distinguish different carbon numbers.

The figures (see below) have been revised to show carbon numbers in color and oxygen numbers in symbols.



11. Table 1: the 3rd column from the right is OH exposure, not OH.

This has been corrected.

12. Table 1: the initial NO and NO₂ concentrations should be given here, given their importance. The NO and NO₂ concentrations along with the CO concentrations have been included in Table 1.

13. Tables 2 and 3: many references in these tables are not listed on the reference list. The missing references have been added to the references list.

14. Equation 3: a parameter, A_s, seems to be explained as “A₃” in the text. Please maintain the consistency.

The variable A_s in equation 3 should have been A₃. This has been corrected.

15. Line 330: although spelled out in a table caption, “DPF+DOC” still needs to be spelled out here.

The following detail about the DPF+DOC was added in Section 2.1: “The engine was run at two different loads (idle and 50% load) with two different fuels (diesel and biodiesel), and with and without an aftertreatment system. The aftertreatment system included a diesel oxidation catalyst (DOC) to oxidize CO and THC and a diesel particle filter (DPF) to trap fine particles.”.

16. Line 455: a fractional bias < -100% does not look appropriate, although I understand what the authors mean. I suggest comparing them in log scale or using ratio instead of bias.

Fractional bias and fractional error are statistical metrics very commonly used to evaluate model predictions in the air quality and atmospheric chemistry community. The fractional bias can vary from -200% to +200% while the fractional error varies between 0% to 200%. An under-prediction of a factor of 2 translates to a fractional bias of -67%, an under-prediction of a factor of 5 translates to a fractional bias of -133%, and an under-prediction of a factor of 10 translates to a fractional bias of -163%. We have added the formulae for fractional bias and fractional error where we discuss these statistical metrics for the first time: “statistical metrics of fractional bias, fractional error, and R² for the comparison for both models are listed in Table S4 (fractional bias = $\frac{1}{N} \sum_{i=1}^n \frac{M-O}{M+O}$, fractional error = $\frac{1}{N} \sum_{i=1}^n \frac{|M-O|}{M+O}$, M=predicted value, O=observed value, N=sample size)”.

17. Figure 7d: the colors of the dashed lines are not correct.

The colors of the dashed lines are deliberately lighter to separate them from the base case simulation result. This fact has been added to the caption: “The dashed lines in panel (d) are deliberately lighter in color than the solid line to help differentiate the Base result from the sensitivity results.”.

18. Figure 8a: the exponent of “10¹” in the x-axis is covered.

This has been fixed in the new figure.

Modeling the Formation and Composition of Secondary Organic Aerosol from Diesel Exhaust Using Parameterized and Semi-Explicit Chemistry and Thermodynamic Models

Sailaja Eluri¹, Christopher D. Cappa², Beth Friedman³, Delphine K. Farmer³, and Shantanu H. Jathar¹

¹ Department of Mechanical Engineering, Colorado State University, Fort Collins, CO, USA, 80523

² Department of Civil and Environmental Engineering, University of California Davis, Davis, CA, USA, 95616

³ Department of Chemistry, Colorado State University, Fort Collins, CO, USA, 80523

Correspondence to: Shantanu H. Jathar (shantanu.jathar@colostate.edu)

Abstract

Laboratory-based studies have shown that combustion sources emit volatile organic compounds that can be photo-oxidized in the atmosphere to form secondary organic aerosol (SOA). In some cases, this SOA can exceed direct emissions of primary organic aerosol (POA). Jathar et al. (2017) recently reported on experiments that used an oxidation flow reactor (OFR) to measure the photochemical production of SOA from a diesel engine operated at two different engine loads (idle, load), two fuel types (diesel, biodiesel) and two aftertreatment configurations (with and without an oxidation catalyst and particle filter). In this work, we used two different SOA models, the volatility basis set (VBS) model and the statistical oxidation model (SOM), to simulate the formation and composition of SOA for those experiments.

Leveraging recent laboratory-based parameterizations, both frameworks accounted for a semi-volatile and reactive POA; SOA production from semi-volatile, intermediate-volatility, and volatile organic compounds (SVOC, IVOC and VOC); NO_x-dependent parameterizations, multigenerational gas-phase chemistry; and kinetic gas/particle partitioning. Both frameworks demonstrated that for model predictions of SOA mass to agree with measurements across all engine load-fuel-aftertreatment combinations, it was necessary to model the kinetically-limited gas-particle partitioning in OFRs as well as account for SOA formation from IVOCs, which were on average found to account for 70% of the model-predicted SOA. Accounting for IVOCs however resulted in an average under-prediction of 28% for OA atomic O:C ratios. Model predictions of the gas-phase organic compounds (resolved in carbon and oxygen space) from the SOM compared favorably to gas-phase measurements from a Chemical Ionization Mass Spectrometer (CIMS), substantiating the semi-explicit chemistry captured by the SOM. Model-measurement comparisons were improved on using vapor wall-loss corrected SOA parameterizations. As OFRs are increasingly used to study SOA formation and evolution in laboratory and field environments, models such as those developed in this work can be used to interpret the OFR data.

Comment [Office1]: Sailaja: this needs to come from a comment made later.

Deleted: more than 90

Deleted: X

Deleted: a factor of two

Deleted: X

Comment [Office2]: Sailaja: this needs to come from a comment made later.

40 **1 Introduction**

41 Combustion-related aerosols are an important contributor to urban and global air pollution and have
42 impacts on climate ([Pachauri et al., 2014](#)) and human health ([Anderson et al., 2012](#)). While direct particle
43 emissions from combustion sources are dominated by primary organic aerosol (POA) and black carbon
44 ([Bond et al., 2004](#)), these sources also emit more volatile organic compounds (VOCs) that can
45 photochemically react in the atmosphere to form secondary organic aerosol (SOA) ([Robinson et al.,
46 2007](#)). SOA production from combustion emissions is poorly understood and not very well represented in
47 models in terms of its precursors, gas-particle partitioning, composition, and properties ([Fuzzi et al.,
48 2015](#)). Atmospheric models frequently under-predict SOA mass concentrations during strong
49 photochemical episodes in urban areas ([Jathar et al., 2017b](#)), which likely highlights the challenge in
50 modeling the SOA contributions from urban, combustion-related emissions ([Ensberg et al., 2014](#)).

51
52 Diesel-powered sources, which are an important source of air pollution at urban and regional scales, emit
53 precursors that form SOA in the atmosphere ([Gentner et al., 2016](#)). [Robinson et al. \(2007\)](#) found that
54 photochemical processing of exhaust emissions from a small off-road diesel engine led to SOA
55 production and doubled the primary aerosol mass over a few hours in an environmental chamber. [Chirico
56 et al. \(2010\)](#) and [Gordon et al. \(2014\)](#) performed similar chamber experiments on tailpipe emissions from
57 in-fleet, on-road diesel vehicles run on chassis dynamometers. Both found SOA production that was
58 roughly consistent with the findings from [Robinson et al. \(2007\)](#). They additionally found that the use of
59 aftertreatment devices (diesel oxidation catalysts and diesel particulate filters) substantially reduced SOA
60 production (mimicking the reduction in primary aerosol emissions) but observed some SOA production
61 during cold starts and/or regeneration events when the proper functioning of the aftertreatment devices
62 was limited. Furthermore, [Gordon et al. \(2014\)](#) found negligible differences in the SOA formation
63 between diesel and biodiesel fuel. To access longer equivalent photochemical aging timescales compared
64 to typical chamber experiments, [Tkacik et al. \(2014\)](#) measured SOA formation using an oxidation flow
65 reactor (OFR) from air sampled from a highway tunnel in Pittsburgh, PA used by both on-road gasoline
66 and diesel vehicles. OFRs use high concentrations of atmospheric oxidants, e.g. hydroxyl radicals, to
67 achieve long exposures on short actual timescales; further discussion is provided below. [Tkacik et al.
68 \(2014\)](#) measured much stronger SOA formation compared to chambers (SOA: POA was 10:1) over
69 photochemical exposures equivalent to 2 to 3 days, but found that the SOA was lost, or destroyed, as the
70 mixture continued to age over the timescale of a week. Recently, [Jathar et al. \(2017a\)](#) performed
71 experiments using an oxidation flow reactor to measure the photochemical production of SOA from an
72 off-road diesel engine operated at various engine load, fuel, and aftertreatment configurations. [Jathar et al.](#)

73 (2017a) found that efficient combustion at higher engine loads and removal of SOA precursors by
74 aftertreatment systems reduced SOA production by factors of 2 to 10. The only exception was that the
75 aftertreatment system did not seem to reduce SOA production at idle loads possibly because the exhaust
76 temperatures were low enough to limit removal of SOA precursors in the oxidation catalyst. Overall,
77 these studies indicate that diesel exhaust contributes to atmospheric SOA production, although the precise
78 production of SOA varies across dimensions of photochemical age, engine duty cycle, use of alternative
79 fuels, and aftertreatment devices.

80
81 Oxidation flow reactors are being used to study the photochemical production of SOA from both
82 anthropogenic (e.g., Ortega et al. (2016)) and natural (e.g., Palm et al. (2016)) sources. Most OFRs used
83 for SOA studies are 10 to 15 L, flow-through metal reactors with lamps that can produce high
84 concentrations of atmospheric oxidants to simulate photochemical processing (e.g., Lambe et al. (2011)).
85 Flows through an OFR allow for residence times between one and four minutes, but given the high
86 oxidant concentrations OFRs can simulate several weeks of photochemistry. OFRs have three distinct
87 advantages over environmental chambers. First, OFRs are smaller in size and easier to operate than
88 environmental chambers, which allows for shorter experiments and makes them ideal for field
89 deployments (Palm et al., 2016; Simonen et al., 2017). Second, production of high oxidant concentrations
90 in OFRs allows for much longer photochemical exposures (~factor of 10) than those possible with
91 chambers (Lambe et al., 2011). Third, due to their flow-through nature, OFRs have shorter residence
92 times than conventional chambers (~1-4 minutes) and hence are less susceptible to gas and particle losses
93 that can influence SOA formation (Zhang et al., 2014; Krechmer et al., 2016). Despite those advantages,
94 there are concerns that the accelerated chemistry and limitations to gas/particle partitioning may affect the
95 formation and composition of SOA in OFRs, which calls into question their relevance in understanding
96 SOA formation in the real atmosphere (Palm et al., 2016; Jathar et al., 2017a; Ahlberg et al., 2017). For
97 example, short residence times and/or small condensation sinks from preexisting aerosol may not allow
98 for complete condensation of SOA vapors (Lambe et al., 2015). Similarly, high oxidant concentrations in
99 OFRs may lead to molecules undergoing a greater number of reactions in the gas-phase before
100 condensing, including reactions that lead to fragmentation and formation of higher volatility products
101 (Kroll et al., 2009). Both effects will typically suppress SOA production. With the increased use of OFRs,
102 there is a need to develop and use modeling tools that can account for fragmentation reactions and kinetic
103 gas/particle partitioning. This will allow for a more accurate interpretation of OFR data and facilitate
104 translation of OFR results to the real atmosphere.

105

Deleted: three

Deleted: up to two weeks

Deleted: 3

109 Models used to simulate the photochemical production of SOA from VOCs in combustion emissions have
110 traditionally used the two-product (Odum et al., 1996) or the more generalized n-product volatility basis
111 set (VBS) framework (Donahue et al., 2006a). In this framework, VOC oxidation products are lumped
112 into volatility bins based on their effective saturation concentrations (C^*) and where the saturation
113 concentration determines the partitioning of the products between the gas and particle phases (Pankow,
114 1994). This framework has been widely used in both box (Dzepina et al., 2009; Hodzic et al., 2010; Jathar
115 et al., 2014a; Hayes et al., 2015) and three-dimensional (Murphy and Pandis, 2009; Tsimpidi et al.,
116 2009; Jathar et al., 2011; Ahmadov et al., 2012; Kononov et al., 2015) models to simulate the chemistry
117 and gas/particle partitioning of SOA. While this framework offers a simple and computationally efficient
118 scheme to model SOA formation, the use of volatility alone neither tracks the molecular composition, nor
119 informs the continued multi-generational chemistry that will determine the atmospheric evolution and
120 properties of SOA. As a result, volatility-based models have been challenged in leveraging observations
121 of the elemental composition of SOA (e.g., atomic O:C ratios) that have become possible through the use
122 of the aerosol mass spectrometer (AMS) to constrain parameterizations or test model predictions. Further,
123 most volatility-based models have employed *ad hoc* parameterizations to model multi-generational
124 chemistry that do not account for fragmentation reactions (Robinson et al., 2007) and possibly double
125 count SOA formation (Jathar et al., 2016). Therefore, there is a demand to develop models that can
126 provide an improved representation of the chemistry that governs the formation, composition, and
127 properties of SOA.

128
129 Previously, volatility-based SOA models have been used to predict photochemical production of SOA
130 from motor vehicle exhaust (Robinson et al., 2007; Jathar et al., 2014b; Tkacik et al., 2014). These
131 modeling studies have shown that speciated SOA precursors such as long alkanes (C_{6-12}) and single-ring
132 aromatics (e.g., benzene, toluene) explain less than 20% of the observed SOA and have argued that the
133 remainder of the SOA (~80%) arises from the photooxidation of typically unspciated organic
134 compounds. These unspciated compounds, also referred to as intermediate volatility organic compounds
135 (IVOCs), are likely species with carbon numbers larger than 12 and appear as an unresolved complex
136 mixture on using traditional gas chromatography mass spectrometry (GC-MS) techniques (Presto et al.,
137 2011). Early estimates of IVOC emissions and their SOA potential have significantly improved
138 predictions of the SOA formed from diesel exhaust (Jathar et al., 2014b) and have broadly improved OA
139 model performance in three-dimensional large-scale models (Murphy and Pandis, 2009; Pye and Seinfeld,
140 2010; Jathar et al., 2011; Tsimpidi et al., 2009). Consider as an example that Zhao et al. (2015), using a
141 thermal desorption GC-MS to provide detailed speciation of the carbon-number resolved linear, branched,

142 and cyclic alkane IVOCs in diesel exhaust, found that these species accounted for up to 60% of the non-
143 methane organic gas emissions. While IVOCs have been recognized as an important class of SOA
144 precursors for diesel (and even for gasoline and biomass burning) sources, updated emissions and
145 speciation estimates from [Zhao et al. \(2015\)](#) have not yet been used to explain observations of
146 photochemically produced SOA from diesel exhaust.

147
148 Recently, several model frameworks have been developed to improve the representation of SOA
149 formation, considering dimensions of SOA beyond just volatility. The statistical oxidation model (SOM)
150 developed by [Cappa and Wilson \(2012\)](#) is one such example, although volatility remains an important
151 consideration. The SOM is a semi-explicit, parameterizable mechanism that uses a two-dimensional
152 carbon-oxygen grid to simulate the multigenerational chemistry and gas/particle partitioning of organic
153 compounds. Although the SOM does not explicitly track or specify the product species composition (e.g.,
154 functional groups), the carbon- and oxygen-number representation provides adequate detail to represent
155 many key atmospheric processes, e.g., reactions with oxidants, formation of functionalized products,
156 scission of carbon backbones or fragmentation, surface and condensed-phase chemistry and gas/particle
157 partitioning. The SOM has been used to interpret chamber experiments ([Zhang et al., 2014](#); [Cappa et al.,
158 2013](#); [Cappa and Wilson, 2012](#)) and was recently integrated into a chemical transport model ([Jathar et al.,
159 2015](#)) to examine the influence of multigenerational aging ([Jathar et al., 2016](#)) and chamber-based vapor
160 wall losses ([Cappa et al., 2016](#)) on ambient concentrations and properties of OA. The two-dimensional
161 VBS (2D-VBS) of [Donahue et al. \(2011\)](#) and the carbon-polarity grid of [Pankow and Barsanti \(2009\)](#) are
162 examples of similar frameworks. These more sophisticated models (i.e., SOM, 2D-VBS, carbon-polarity
163 grid) have not yet been employed to study SOA formation from complex mixtures such as combustion
164 emissions.

165
166 To summarize, combustion sources such as diesel-powered sources emit precursors that can photooxidize
167 in the atmosphere to produce SOA. This SOA production is dependent not only on the precursor
168 composition (that could vary by combustion mode and fuel type) and photochemical age, but also
169 experimental artifacts (e.g., short condensation timescales) introduced by oxidation flow reactors. Hence,
170 there is a need to develop and apply sophisticated, yet computationally efficient, numerical models to
171 simulate and study SOA formation from combustion emissions. In this work, we applied two SOA model
172 frameworks that vary in sophistication (VBS and SOM) to simulate the photochemical production of SOA
173 in an OFR from diesel exhaust. The models were evaluated by comparing model predictions (OA and
174 O:C) to the recent measurements made by [Jathar et al. \(2017a\)](#) where SOA production was quantified for

175 different photochemical ages under varying engine loads, fuels, and aftertreatment devices. The model-
176 measurement comparison, along with sensitivity simulations, highlights the importance of modeling the
177 kinetic gas/particle partitioning of SOA in OFRs, the contribution of IVOCs to the total SOA production,
178 and the ability of the SOM to accurately track the composition of SOA.

179

180 2 Methods

181 2.1 Experiments and Data

182 [Jathar et al. \(2017a\)](#) performed photooxidation experiments using an OFR to measure SOA production
183 from the exhaust of a 4.5L, John Deere diesel engine. The stock engine met Tier 3 emissions standards for
184 off-road diesel engines. The OFR used therein was described in detail by [Friedman et al. \(2016\)](#) and the
185 experimental setup and OA measurements from these experiments were described in detail by [Jathar et al.](#)
186 [\(2017a\)](#). We briefly summarize the experimental setup, measurements, and findings from [Jathar et al.](#)
187 [\(2017a\)](#). The engine was run at two different loads (idle and 50% load) with two different fuels (diesel
188 and biodiesel), and with and without an aftertreatment system. The aftertreatment system included a diesel
189 oxidation catalyst (DOC) to oxidize CO and THC and a diesel particle filter (DPF) to trap fine particles.
190 Diesel exhaust was diluted by a factor of 45-110 before entering the OFR. The intensity of the mercury
191 lamps (at wavelengths of 185 and 254 nm) inside the OFR was varied to produce different hydroxyl
192 radical (OH) concentrations and simulate different photochemical exposures. The OFR had a residence
193 time of 100 s. A suite of instrumentation was used to measure gas- (CO₂, CO, total hydrocarbons, NO_x,
194 O₂, oxygenated organic compounds) and particle- (aerosol size and composition) phase concentrations. A
195 total of fourteen experiments (see Table 1 for more details) were performed at varying engine loads and
196 with varying fuels and aftertreatment configurations. The OH exposure was varied between 0 and a
197 maximum of 9.2×10^7 molecules-hr cm⁻³ (equivalent to 2 days of photochemical aging at an OH
198 concentration of 1.5×10^6 molecules cm⁻³). On average, each experiment included measurements at six to
199 seven different photochemical exposures. The mass concentrations and elemental composition of the POA
200 (measured when OFR lights were off) and SOA (at varying OH exposures) were measured by a high-
201 resolution aerosol mass spectrometer (HR-AMS). In addition to the measurements reported by [Jathar et al.](#)
202 [\(2017a\)](#), the gas-phase concentrations of oxygenated organic compounds were measured by an acetate
203 reagent ion-based chemical ionization mass spectrometer (CIMS) ([Link et al., 2016](#)). At all engine
204 configurations, SOA production exceeded the POA emissions after the equivalent of a few hours of
205 atmospheric photochemical aging. SOA production was particularly strong at idle (or less fuel-efficient)
206 engine loads and/or when exhaust temperatures were low and proper functioning of the aftertreatment
207 devices was limited. Further, POA emissions and SOA production were nearly identical between diesel

208 and biodiesel fuels. A synopsis of experiments performed and the total hydrocarbons (THC), which
209 includes all SOA precursors, POA, SOA, O:C, OH, and size distribution data are presented in Table 1.

Deleted: the
Deleted: (
Deleted:)

211 Although the diesel exhaust was diluted with clean air to produce atmospherically-relevant concentrations
212 of POA, the initial THC, CO, and NO_x concentrations in the OFR were still quite high. Peng and Jimenez
213 (2017), using a detailed gas-phase model, argued that the high external OH reactivity from high THC,
214 CO, and NO_x concentrations might lead to non-OH chemistry in the OFR and NO could quickly be
215 consumed in the OFR leading to low NO conditions for SOA formation. Peng and Jimenez (2017)
216 quantified the potential influence of NO on the oxidation chemistry by calculating the ratio of the reactive
217 flux of the peroxy radicals with NO to the reactive flux of the peroxy radicals with HO₂ ($r_{RO_2+NO}/r_{RO_2+HO_2}$).
218 A ratio greater than 1 was considered as “high NO” while a ratio less than 1 was considered “low NO”.
219 For the relative humidity, photon flux, initial NO, and external OH reactivity values in Jathar et al.
220 (2017a), the model of Peng and Jimenez (2017) predicted that the OFR mostly ran in a high NO mode at
221 all photochemical exposures when the engine was run at load conditions or with an aftertreatment device
222 in place. However, the model predicted that the OFR mostly ran in a low NO mode especially at the high
223 photochemical exposures when the engine was run at idle conditions and without an aftertreatment device
224 (i.e., Idle-Diesel-None and Idle-Biodiesel-None). The $r_{RO_2+NO}/r_{RO_2+HO_2}$ ratio and low versus high NO
225 mode for each photon flux-experiment combination is listed in Table S1. Based on these results, we
226 accordingly used the low and high NO_x parameterizations to perform the model simulations.

Deleted: HO₂
Deleted: NO

Deleted: HO₂
Deleted: NO
Deleted: experiment and photochemical exposure

228 2.2 Organic Aerosol Models

229 In this work, we used two different OA models to predict the mass concentrations and chemical
230 composition of SOA and compare predictions against the SOA measurements from [Jathar et al. \(2017a\)](#)
231 and [Friedman et al. \(2017\)](#). In this section, we briefly describe the two model frameworks, namely the
232 Volatility Basis Set (VBS) and the Statistical Oxidation Model (SOM), used to simulate the coupled
233 chemistry, thermodynamic properties, and kinetic gas/particle partitioning of OA. The VBS model was
234 chosen as it is widely used in contemporary air quality models; the SOM was chosen to examine the
235 influence of improved representation of OA processes (e.g., fragmentation reactions) on model
236 predictions.

238 2.2.1 Volatility Basis Set

239 The Volatility Basis Set model, developed by [Donahue et al. \(2006b\)](#), is a parameterizable model that
240 allows for a volatility-based representation of the coupled chemistry, thermodynamic properties, and

249 gas/particle partitioning of OA. The VBS uses logarithmically spaced so-called basis sets based on the
250 effective saturation concentration (C^*); C^* of a species determines the partitioning between the gas and
251 particle phases (Pankow, 1994). In the VBS model, organic precursors were allowed to react with OH to
252 yield a unique product distribution in C^* space that represented stable first-generation products.

253 Subsequent multi-generational gas-phase oxidation, or so-called ‘aging,’ of the VBS products was
254 modeled using the scheme of Robinson et al. (2007). In this scheme the product species are allowed to
255 react with OH and yield a product with a C^* that is an order of magnitude lower than the direct precursor,
256 to a lower limit C^* of $10^{-2} \mu\text{g m}^{-3}$. This scheme did not consider fragmentation reactions. The following
257 equations were used to represent the organic precursor oxidation (equation 1) and subsequent reaction and
258 formation of products from the precursor oxidation and aging reactions (equation 2):

$$259 \frac{dV}{dt} = -k_{OH}[V][OH] \quad (1)$$

$$260 \frac{dC_j^{g+p}}{dt} = \alpha_j k_{OH}[V][OH] + \beta k_{OH,aging}[C_{j+1}^g][OH] - \gamma k_{OH,aging}[C_j^g][OH] \quad (2)$$

261 where V is the gas-phase concentration of a generic organic precursor ($\mu\text{g m}^{-3}$; includes VOCs, IVOCs
262 and SVOCs), k_{OH} is the reaction rate constant between the precursor and OH ($\text{cm}^3 \text{ molecule}^{-1} \text{ s}^{-1}$), C_j^{g+p}
263 is the gas + particle-phase concentration in the j^{th} bin ($\mu\text{g m}^{-3}$), α_j is the mass yield of the first-generation
264 oxidation product of the j^{th} bin (Table 2), $k_{OH,aging}$ is the reaction rate constant ($\text{cm}^3 \text{ molecule}^{-1} \text{ s}^{-1}$) to
265 represent multi-generational aging of the oxidation products, and β and γ are the mass yields associated
266 with the production and loss terms from multi-generational aging. For the j^{th} bin, the second term in
267 equation (2) represents the formation of oxidation products from the $j+1^{\text{th}}$ volatility bin and the third term
268 in equation (2) represents the loss of precursor from the j^{th} bin. β and γ are assumed to have a value of 1
269 (meaning no fragmentation) but β is zero for the last bin and γ is zero for the first bin.

270
271 Volatility-resolved mass yields for eighteen different organic precursors for C^* bins ranging from 10^{-1} to
272 $10^3 \mu\text{g m}^{-3}$ were adopted or refit based on low and high NO_x parameterizations published in the literature;
273 organic precursors, the high and low NO_x VBS mass yields, and the relevant references are listed in
274 Tables 2 and 3. Since there were no direct low NO_x VBS parameterizations for alkanes, parameterizations
275 for linear, branched, and cyclic alkanes were developed using pseudo chamber data generated with the
276 SOM based on the low NO_x parameters listed in Table 5, for *n*-dodecane, methylundecane, and
277 hexylcyclohexane respectively. Some of these parameterizations accounted for vapor wall losses and have
278 been accordingly marked in Tables 2 and 3. Each SOA precursor in the exhaust emissions was assigned a
279 surrogate from Table 2/3 to model SOA formation in the VBS model. When using the high NO_x

Deleted: VOCs

Deleted: was

Deleted: 1

Deleted: VOC

Deleted: VOC

Deleted: VOC

Deleted: here, VOC

Deleted: VOC

Deleted: VOCs

Deleted: VOCs

Deleted: their

Deleted: 3

Deleted: (more details can be found in the supplementary material)

Deleted:

parameterizations, branched and cyclic alkanes were assigned surrogates based on equivalent linear alkanes, following the work of Lim and Ziemann (2009) and Tkacik et al. (2012). A C_X branched alkane was assigned a C_{X-2} linear alkane as a surrogate and a C_X cyclic alkane was assigned a C_{X+2} linear alkane as a surrogate. Since we only fit alkanes up to *n*-heptadecane, we considered *n*-heptadecane as a surrogate for alkanes C₁₇-C₂₂. The Idle-Diesel-None and Idle-Biodiesel-None experiments used the low NO_X parameterizations while all the other experiments used the high NO_X parameterizations. The mass transfer (condensation/evaporation) of the VBS products to the particle phase was assumed to be kinetically-limited in the OFR (Palm et al., 2016; Jathar et al., 2017a; Ahlberg et al., 2017); Section 2.3 describes the mass transfer equation used to model kinetic gas/particle partitioning.

Deleted: B

2.2.2 Statistical Oxidation Model

The Statistical Oxidation Model (SOM), developed by Cappa and Wilson (2012) is a semi-explicit, parameterizable model that allows for a statistical representation of the coupled chemistry, thermodynamic properties, and gas/particle partitioning of OA. The SOM uses a 2-dimensional carbon-oxygen grid to track gas- and particle-phase precursors and products from precursor oxidation. Each cell in the SOM grid represents a model organic species with a molecular weight defined by the formula C_xH_yO_z. A SOM species reflects the average properties (e.g. C*, reactivity) of all actual species with the same number of carbon (N_C) and oxygen (N_O) atoms that are produced from a given precursor class (e.g., benzene, alkanes). In the SOM, all gas-phase species are assumed to be reactive towards OH and the OH reaction rate constant (k_{OH}) is calculated using equation 3 as follows:

Deleted: VOC

$$\log(k_{OH}) = A_1 + A_2 \times (N_C^{A_3}) \times \exp\left(-1 \times \frac{E_a}{8.314 \times T}\right) \times \left[1 + \frac{b_1}{\sigma \sqrt{2\pi}} \exp\left(-\frac{1(\ln(N_O+0.01)-\ln(b_2))^2}{2\sigma^2}\right)\right] \quad (3)$$

Deleted: reactivity

Deleted: S_{OH}

$$\sigma(N_C \leq 15) = 0.0214 \times N_C + 0.5238$$

$$\sigma(N_C \geq 15) = -0.115 \times N_C + 2.695$$

$$b_1 = -0.2583 \times N_C + 5.8944$$

$$b_2(N_C \leq 15) = 0.0314 \times N_C + 0.9871; \quad b_2(N_C > 15) = 0.25 \times N_C - 2.183$$

where A₁=15.1, A₂=3.94, and A₃=0.797. k_{OH} for a specified N_C and N_O is assumed to be the same for species in all the SOM grids.

The reactions with OH lead to either functionalization or fragmentation, resulting in movement through the carbon-oxygen grid. Six precursor-specific adjustable parameters are assigned for each SOM grid: four parameters that define the molar yields of the four functionalized, oxidized products (p_{O,k}, Σp_{O,k}=1 and hence one out of the four parameters is determined by mass balance), one parameter that determines

331 the probability of functionalization or fragmentation (P_{Frag} , $P_{Func}=1-P_{Frag}$) and one parameter that
 332 describes the change in C^* associated with the addition of one oxygen atom (ΔLVP). Equation 4
 333 represents the evolution of species in the SOM grid:

$$334 \frac{d[C_X O_Z]}{dt} = -k_{OH}^{X,Z} [OH][C_X O_Z] + [OH] \sum_{k=1}^4 k_{OH}^{X,Z-k} P_{func}^{X,Z-k} p_{O,k} [C_X O_{Z-k}] +$$

$$335 [OH] \sum_{j=1}^{j_{max}} \sum_{k=0}^{k_{max}-Z} k_{OH}^{X+j,Z-1+k} \frac{P_{frag}^{X,Z-1+k}}{N_{fragments}^{X,Z}} [C_X O_{Z-1+k}] \quad (4)$$

336 where $C_X O_Z$ is the gas + particle-phase concentration of the SOM species with X carbon atoms and Z
 337 oxygen atoms ($\mu\text{g m}^{-3}$) and $N_{fragments}$ is the number of possible products from fragmentation. The
 338 probability of fragmentation is modeled using equation 5 as a function of the O:C ratio because higher
 339 O:C ratio compounds are expected to have a higher probability of fragmentation ([Chacon-Madrid and](#)
 340 [Donahue, 2011](#)):

$$341 P_{frag} = \left(\frac{N_O}{N_C}\right)^{m_{frag}} \quad (5)$$

342 The C^* for each SOM species was calculated using equation 6 as follows:

$$343 \log_{10} C^* = -0.337 MW_{HC} + 11.56 - (N_O \times \Delta LVP) \quad (6)$$

344 where MW_{HC} (g mole^{-1}) is the molecular weight of the hydrocarbon backbone (accounting only for the
 345 carbon and hydrogen atoms).

346
 347 The parameters used to model SOA formation were based on those published in [Cappa et al. \(2016\)](#) and
 348 are listed in Tables 4 and 5. These parameter sets were developed by fitting the SOM predictions to
 349 chamber measurements of SOA mass concentrations and include corrections to account for vapor wall
 350 losses ([Zhang et al., 2014](#)). Each SOA precursor in the exhaust emissions was assigned a surrogate from
 351 Table 4 or 5 to account for the oxidation chemistry associated with oxidation of that species. For example,
 352 pentadecane used the parameterization developed by fitting n -dodecane. The difference in the initial
 353 number of carbons and oxygens, and thus the volatility, between the surrogate compound and the
 354 precursor compound of interest was accounted for, with consequent impact on the SOA yield. In other
 355 words, unlike the VBS where the SOA mass yield of the SOA precursor and surrogate is identical, the
 356 surrogate in the SOM only informed the statistical trajectory for multi-generational oxidation of a given
 357 precursor, and the surrogate and actual compound of interest can have different SOA mass yields. [The](#)
 358 [Idle-Diesel-None and Idle-Biodiesel-None experiments used the low NO_x parameters while all the other](#)
 359 [experiments used the high NO_x parameters](#). Similar to the VBS model, the mass transfer
 360 (condensation/evaporation) of the SOM products to the particle phase was assumed to be kinetically-
 361 limited in the OFR ([Palm et al., 2016](#); [Jathar et al., 2017a](#); [Ahlberg et al., 2017](#)) and Section 2.3 below

Deleted: 3

Deleted: at high NO_x concentrations

Deleted: 3

365 describes the mass transfer equation used to model kinetic gas/particle partitioning.

366

367 2.3 Kinetic Gas/Particle Partitioning

368 [Palm et al. \(2016\)](#), [\(Ahlberg et al., 2017\)](#), and [Jathar et al. \(2017a\)](#) have argued that the short residence
369 times and small condensation sinks in the OFR may not permit all low-volatility products formed from
370 [precursor](#) oxidation to condense onto preexisting aerosol. Hence, unlike earlier work that has assumed
371 equilibrium partitioning to model SOA in OFRs ([Tkacik et al., 2014](#); [Chen et al., 2013](#)), we modeled the
372 kinetic gas/particle partitioning of OA using equation 7 ([Zhang et al., 2014](#)):

$$373 \frac{dc_i^p}{dt} = 2\pi D_i D_p N_p F_{FS} (C_i^g - \frac{c_i^p c_i^*}{C_{OA}}) \quad (7)$$

374 where C_i^p is the particle-phase mass concentration for the i^{th} organic species ($\mu\text{g m}^{-3}$), D_i is the gas-phase
375 diffusion coefficient of the i^{th} organic species ($\text{m}^2 \text{s}^{-1}$), D_p is the number mean particle diameter (m), N_p is
376 the total particle number concentration (m^{-3}), F_{FS} is Fuchs-Sutugin correction for non-continuum mass
377 transfer, C_i^g is the gas-phase mass concentration of the i^{th} organic species ($\mu\text{g m}^{-3}$), C_i^* is the effective
378 saturation concentration of the i^{th} organic species, and C_{OA} is the total OA mass concentration ($\mu\text{g m}^{-3}$).
379 The i^{th} organic species refers to the organic compounds tracked in the VBS bins and the SOM grids. The
380 gas-phase diffusion coefficient was calculated for each organic species as follows:

$$381 D_i = D_{CO_2} \frac{MW_{CO_2}}{MW_i} \quad (8)$$

382 where D_{CO_2} is the gas-phase diffusion coefficient of CO_2 ($1.38 \times 10^{-5} \text{ m}^2 \text{ s}^{-1}$), MW_{CO_2} (g mole^{-1}) is the
383 molecular weight of CO_2 , and MW_i (g mole^{-1}) is the molecular weight of the i^{th} organic species. In the
384 VBS model where we do not track the molecular composition of the SOA species, we assumed all
385 condensing species to have a molecular weight of 200 g mole^{-1} . [This formulation to calculate the gas-](#)
386 [phase diffusion coefficient under-predicted the measured gas-phase diffusion coefficients compiled by](#)
387 [Tang et al. \(2015\) by ~20%. However, doubling the gas-phase diffusion coefficient calculated in equation](#)
388 [8 resulted in very small change \(<1%\) in the OA mass predictions for a representative experiment. Hence,](#)
389 [we decided to use the formulation in equation \(8\) for the rest of this work.](#) The Fuchs-Sutugin correction
390 was calculated as follows:

$$391 F_{FS} = \frac{0.75\alpha(1+Kn)}{Kn^2+Kn+0.283 \cdot Kn \cdot \alpha + 0.75\alpha} \quad (9)$$

$$392 Kn = \frac{2\lambda_i}{D_p} \quad (10)$$

$$393 \lambda_i = \frac{3D_i}{C_i} \quad (11)$$

Deleted: VOC

395
$$C_i = \sqrt{\frac{8N_A k T}{\pi M W_i}} \quad (12)$$

396 where Kn is the Knudsen number, α is the mass accommodation coefficient, λ_i is the mean free path of the
397 i^{th} organic species in air (m), C_i is the root mean square speed of the gas (m s^{-1}), N_A is Avogadro's number
398 ($\text{molecules mole}^{-1}$), k is the Boltzmann constant ($\text{m}^2 \text{kg s}^{-2} \text{K}^{-1}$), and T is the temperature (K).

399

400 2.4 Model Inputs

401 2.4.1 Semi-Volatile and Reactive POA

402 Previous work has shown that much of combustion-related POA is semi-volatile and exists in an
403 equilibrium with gas-phase vapors (Robinson et al., 2007; Huffman et al., 2009; May et al., 2013c, b; May
404 et al., 2013a). Jathar et al. (2017a) measured emissions of POA at no OH exposure and these measured
405 concentrations were used to initialize the seed OA available for partitioning in the OFR and to calculate
406 the mass concentrations of vapors in equilibrium with the POA. The mass concentrations of the POA
407 vapors were determined based on the normalized, volatility-resolved distribution of primary organic
408 compounds estimated by May et al. (2013b) for emissions from a suite of on- and off-road diesel vehicles.
409 The volatility distribution of May et al. (2013b) for diesel primary organic compounds is listed in Table

410 6(a). For the SOM, we assumed that the primary organic compounds could be represented using a
411 distribution of n -alkanes and we refit the volatility distribution in Table 6(a) to develop a carbon-number
412 resolved distribution of n -alkanes; this distribution is listed in Table 6(b).

413

414 2.4.2 SOA Precursors

415 Jathar et al. (2017a) did not speciate the THC or SOA precursor emissions from the diesel engine and
416 hence we have developed our own emissions profiles based on previously published literature to speciate
417 the THC emissions. In this work, we used two different emissions profiles listed in EPA SPECIATE
418 version 4.3 that are commonly used to speciate THC emissions from diesel engines for emissions
419 inventories used in atmospheric modeling (EPA, 2013): Profiles #3161 (Diesel Exhaust- Farm
420 Equipment) and #8774 (Heavy Duty Diesel Exhaust). Profile #3161 best matched the diesel engine source
421 and diesel fuel used by Jathar et al. (2017a) and was used as the baseline emissions profile to speciate the
422 THC emissions; we examined the sensitivity of using Profile #8774 on model predictions. We were
423 unable to find a comprehensive emissions profile for THC emissions from the use of straight biodiesel
424 fuel in the literature, and have relied on emissions profiles that were determined for biodiesel-diesel
425 blends. Profile #4777 (30% Biodiesel Exhaust - Light Duty) was used as the baseline emissions profile to
426 speciate THC emissions for experiments performed using the biodiesel fuel. All three emissions profiles

Deleted: 4

Deleted: 4

Deleted: 4

Deleted: The POA and POA vapors estimated for the VBS and SOM models for all the experiments are listed in the supplementary information (Tables S1 and S2).

433 (3161, 8774, and 4777) are listed in Tables S2 through S4.
434
435 Prior work in studying SOA formation has revealed that traditional speciation of THC emissions does not
436 include emissions of high molecular-weight organic compounds, such as IVOCs, that are important SOA
437 precursors (Jathar et al., 2014b). In Profile #3161 such compounds are partially accounted for in the
438 ‘unknown’ species category (13.76% by mass of THC). Zhao et al. (2015) recently estimated that IVOCs
439 were 60% of the THC emissions from a suite of on- and off-road diesel engines and provided a semi-
440 explicit speciation of the IVOC emissions as a carbon-number distribution of linear, branched and cyclic
441 alkanes. To account for these IVOC emissions, we assumed that the base case emissions profiles
442 contained 30% IVOCs on a mass-basis (this IVOC fraction was selected since it resulted in the most
443 optimum model-measurement comparison for OA mass; this will be discussed later in Section 3.3) and
444 had the same chemical speciation as that proposed by Zhao et al. (2015) for an off-road engine
445 (transportation refrigeration unit). We performed sensitivity simulations using IVOC fractions of 0%
446 (assuming that the THC emissions contained no IVOCs), 13.76% (based on the ‘unknown’ category in
447 Profile #3161), and 60% (based on the median estimate in Zhao et al. (2015)), on a mass-basis. Addition
448 of IVOCs to the emissions profile meant that the VOC species (e.g. benzene, toluene, short alkanes) had
449 to be renormalized to accommodate the IVOCs. Table 7 lists the renormalized baseline emissions profiles
450 for SOA precursors used for diesel and biodiesel exhaust with 30% IVOCs along with the reaction rate
451 constants with OH (k_{OH}) and surrogates (or model compound) used to model SOA formation for the VBS
452 and SOM models. Concentrations for each species were determined by multiplying the experiment-
453 specific THC mass concentrations with the renormalized emissions profiles.

455 2.4.3 Particle Size and Particle Number Concentrations

456 For numerical simplicity, we used a monodisperse aerosol, the properties of which (number mean
457 diameter (D_p) and number concentration (N_p)) were initialized from the measured particle size distribution
458 data when modeling kinetic gas/particle partitioning. For experiments performed without the DPF+DOC,
459 the initial particle number concentrations and condensational sinks were high ($>3.3 \times 10^5 \text{ # cm}^{-3}$ and >0.5
460 min^{-1}) and hence the monodisperse aerosol was initialized based on data at no photochemical exposure.
461 For experiments performed with the DPF+DOC where the initial particle number concentrations were
462 relatively low ($<1000 \text{ # cm}^{-3}$ and $<0.003 \text{ min}^{-1}$), photochemical aging resulted in formation and growth of
463 new particles and provided a substantial increase in the surface area ($>$ factor of 300) available for
464 condensation. In these experiments, we initialized the monodisperse aerosol using an average of the data
465 at no photochemical exposure and after photochemical exposure (Palm et al., 2016). Averaging the data

Deleted: 1

Deleted: 3

Deleted: he magnitude of

Deleted: in

Deleted: baseline

Deleted: s

Deleted: 6

Deleted: , based on the median estimate in Zhao et al. (2015)

Deleted: ,

Deleted: and

Deleted: baseline

Deleted: 5

Deleted: es

Deleted: 6

Deleted: 3

Deleted: 100

482 allowed for a more realistic estimate of the condensational sink. In each simulation, the condensing SOA
483 mass was used to calculate the change in particle size but the number concentration was conserved. The
484 number mean diameter and the number concentration data - representing the initial condensational sink –
485 for all experiments are listed in Table 1.

486
487 New particle formation and growth was observed for most experiments at or near the highest
488 photochemical ages (at or >1 OH day), which presumably influenced the condensational sink at the
489 beginning of the experiment. Therefore, we performed sensitivity simulations to investigate the influence
490 of new particle formation on model predictions. We performed simulations with each model (VBS and
491 SOM) with four different initial condensational sinks. The first three simulations used measured data to
492 calculate the initial condensational sink inputs: (i) number mean diameter and measured number
493 concentration at no OH exposure (equivalent to the default for non-DPF+DOC experiments), (ii) number
494 mean diameter and measured number concentration at the given OH exposure, and (iii) average of (i) and
495 (ii) (default for DPF+DOC experiments). The fourth simulation (iv) assumed that the OFR nucleated 1
496 nm particles at the beginning of the experiment where the number concentration of these particles was
497 equal to that measured at the end of the experiment.

498

499 2.5 Model Simulations and Model Code

500 The VBS and SOM models were run separately for each photochemical exposure simulated for each
501 experiment listed in Table 1. In the VBS simulations, POA was tracked in one basis set while products
502 from each SOA precursor were tracked in separate basis sets, allowing us to distinguish between POA and
503 SOA. In the SOM simulations, all precursor molecules with the same surrogate (e.g., all *n*-alkanes) were
504 tracked in the same SOM grid. Model simulations were performed in phases to answer specific questions
505 and inform model inputs for later simulations:

- 506 1. To provide a general overview of the model predictions and model-measurement comparison, and
507 to orient the reader to the results thereafter, we performed simulations with the VBS and SOM
508 models using the base set of inputs for one of the Idle-Diesel-None experiments. Our base case
509 included: Profile #3161 for VOC emissions, 30% IVOC mass fraction, kinetic gas/particle
510 partitioning with a mass accommodation coefficient of 0.1, and monodisperse aerosol inputs based
511 on measured data at no photochemical exposure. [The partitioning- and IVOC-related choices for](#)
512 [the base case are discussed in Sections 3.2 and 3.3 respectively.](#)
513 2. Models used to simulate SOA production in environmental chambers and OFRs have typically
514 assumed instantaneous equilibrium partitioning (e.g., [Chen et al. \(2013\)](#)). To examine the validity

Deleted: 6

Deleted: IVOC and

Deleted: .

of assuming instantaneous equilibrium partitioning, we performed simulations with the VBS and SOM models using instantaneous or kinetic gas/particle partitioning for one of the Idle-Diesel-None and the Idle-Diesel-DPF+DOC experiments. Kinetic partitioning was modeled using three values of the mass accommodation coefficient ($\alpha=0.01, 0.1, 1$) to capture the uncertainty in its true value. To examine the influence of an increased initial condensational sink from new particle formation on kinetic partitioning, we performed additional simulations using four different initial condensational sinks (see Section 2.4.3) on one of the Idle-Diesel-None and the Idle-Diesel-DPF+DOC experiments.

3. Previous work has shown that combustion-related IVOCs are important precursors of SOA (e.g., Jathar et al. (2014b)). To investigate the importance of IVOCs, we performed simulations with the VBS and SOM models at four different assumed IVOC mass fractions (0%, 13.76%, 30%, and 60%), as discussed above when discussing the THC profiles, at all photochemical exposures and for all the experiments listed in Table 1. We performed additional simulations with different emissions profiles and SOA parameterizations on one of the Idle-Diesel-None experiments to investigate uncertainties linked to the composition and SOA potential of IVOCs.

4. Additional simulations were performed to examine the sensitivity of model predictions to the following processes: multi-generational aging, vapor wall losses, residence time distributions, and spatial heterogeneity in OH concentrations.

The numerical codes for the VBS were developed in Matlab while those for the SOM were developed in IGOR (WaveMetrics Inc.). These codes will be made available on request. The simulations were performed on an Intel i5 processor (1.7 GHz) and required ~10 s to perform a VBS simulation and ~500 s to perform a SOM simulation at a single photochemical exposure.

3. Results

3.1 General Model Results Using the Base Case

In Figure 1, we compare predictions of OA from the VBS and SOM models using the base case to the measurements for the Idle-Diesel-None experiment performed on June 5. Figures 1(a) and 1(b) compare predictions to the measurements in units of $\mu\text{g m}^{-3}$ and g kg-fuel^{-1} , respectively; hereafter we present all mass predictions in units of g kg-fuel^{-1} . For this experiment, the VBS/SOM models over-predicted the OA mass by a factor of 1.9/2.2 at the lowest photochemical exposure (0.06 OH days) and a factor of 1.6/1.8 at the next highest photochemical exposure (0.17 OH days). The over-prediction was because the models significantly over-predicted the SOA formation at these two photochemical exposures. For higher photochemical exposures (>0.5 OH days), both models slightly under-predicted the OA mass but

Deleted: three

Deleted: further

Deleted: , and low NO_x SOA parameterizations.

Deleted: W

Deleted: in Figure 1

Deleted: VBS and SOM

Deleted: an order of magnitude

Deleted: ~3~2

Deleted: lower

Deleted: s

Deleted: 0.06 and

Deleted: performed very well in reproducing

Deleted: evolution

Deleted: with little difference between the VBS and SOM models

566 predictions were still within the measurement uncertainty. Our base case seemed to offer a mixed model-
567 measurement comparison for this specific experiment (i.e., over-prediction at lower photochemical ages
568 and a slight under-prediction at higher photochemical ages) because the 30% IVOC mass fraction used in
569 the base case was optimized to achieve a favorable model-measurement comparison across all
570 experiments at all photochemical exposures. In other words, the over-prediction in this experiment at
571 lower photochemical exposures was probably offset by an under-prediction at similar photochemical
572 exposures for some of the other experiments. It is important to note that the model performance varied
573 across the suite of experiments and this overall model performance is discussed in more detail in Section
574 3.3. The VBS and SOM models predicted that the OA at the maximum photochemical exposure was
575 dominated by SOA produced from VOC and IVOC oxidation (92-93%), which agreed well with the
576 measured composition (see Figure 1(c)). For the measurements, POA was defined as fresh OA while SOA
577 was defined as OA formed in addition to the POA. Furthermore, both models suggested that most of the
578 SOA emanated from the oxidation of IVOCs with only 7-14% resulting from the oxidation of aromatic
579 VOCs and less than 0.6-4% resulting from alkane VOCs smaller than a C₁₂. This dominance of IVOCs in
580 explaining the photochemically produced SOA is in line with previous OFR and chamber studies that
581 have modeled SOA formation from diesel exhaust (Tkacik et al., 2014; Zhao et al., 2015; Jathar et al.,
582 2014b).

584 3.2 Kinetic Gas/Particle Partitioning

585 In Figure 2, we plot predictions from the VBS and SOM models for the Idle-Diesel-None and Idle-Diesel-
586 DPF+DOC experiments assuming instantaneous and kinetic gas/particle partitioning. The two different
587 experiments were deliberately chosen to highlight the role instantaneous partitioning plays at the
588 extremities. We found that for the Idle-Diesel-None experiment, the use of instantaneous partitioning
589 roughly produced the same result as kinetic partitioning with α values of 0.1 and 1 and that all these
590 predictions resulted in roughly the same model-measurement comparison. The instantaneous partitioning
591 predictions were slightly higher than the kinetic partitioning predictions for the VBS simulations. The
592 kinetic partitioning simulations (except for that with an α of 0.01) produced the same result as the
593 instantaneous partitioning simulation most likely because the initial condensational sink was large enough
594 (1.12 min⁻¹) in this experiment that there were no kinetic limitations to partitioning. The increase in the
595 condensational sink through condensation of SOA (10 min⁻¹ at the highest photochemical exposure)
596 tended to further reduce any differences in the predictions between the kinetic and instantaneous
597 partitioning simulations. However, for the Idle-Diesel-DPF+DOC experiment, the instantaneous
598 partitioning simulation predicted substantial OA mass at the lower photochemical exposures (0.04 and

Deleted: Although
Deleted: o
Deleted: reasonable

Deleted: T
Deleted: , the
Deleted: did vary
Deleted: , which is
Deleted:
Deleted: 3
Deleted: 4

Deleted: about 3-4
Deleted: 1

Deleted: S
Deleted: production

613 0.12 OH days) compared to the kinetic partitioning simulations, specifically a factor of 9.8-29 larger at
614 0.04 OH days and a factor of 9.7-75, larger at 0.12 OH days for the VBS model and a factor of 3.9-5.8
615 larger at 0.04 OH days and a factor of 6.4-9.1 larger for the SOM. The instantaneous partitioning
616 simulations predicted a lot more SOA because all condensable products of organic precursor oxidation
617 were allowed to condense instantaneously (according to their respective volatilities) while the kinetic
618 partitioning simulations predicted little SOA production because the initial condensational sink was quite
619 small (0.002 min^{-1}). Predictions from the instantaneous and kinetic partitioning simulations were much
620 closer at the higher photochemical exposures because the SOA formed had grown the condensational sink
621 enough to reduce limitations to partitioning (1 min^{-1} at the highest photochemical exposure). These results
622 imply that the condensation of SOA in OFRs, in some instances, could be kinetically-limited and that
623 instantaneous partitioning may result in models over-predicting the condensation and formation of SOA.

624
625 We make two additional observations based on the results in Figure 2. First, the initial condensational
626 sink for the Idle-Diesel-None experiment was large (1.12 min^{-1}) compared to condensational sinks one
627 would encounter in the real atmosphere. For example, $5 \mu\text{g m}^{-3}$ of aerosol in a representative rural or
628 remote environment will have a condensational sink $<0.05 \text{ min}^{-1}$ (Seinfeld and Pandis, 2006). Therefore,
629 modeling ambient applications of the OFR or OFR use with sources that use emissions control devices
630 will need to be even more mindful of the instantaneous partitioning assumption while predicting SOA
631 formation. Second, for the kinetic partitioning results, predictions from both models were relatively less
632 sensitive to α values between 0.1 and 1 but were dramatically lower for an α value of 0.01; more than a
633 factor of 2 for the Idle-Diesel-None experiment and more than an order of magnitude for the Idle-Diesel-
634 DPF+DOC experiment. Given the low sensitivity to α values greater than 0.1 and the reasonable model-
635 measurement comparison at an α value of 0.1 and 1 at least for the Idle-Diesel-None experiment, we
636 argue that the SOA condensation can be represented by an α value larger than 0.1 for the OFR
637 experiments in this work. This α value for diesel exhaust SOA was consistent with prior estimates of the α
638 value for biogenic SOA estimated from chamber, OFR, and aerosol heating experiments (Lee et al.,
639 2011; Saleh et al., 2013; Karnezi et al., 2014; Palm et al., 2016) and direct measurements of α for alkanol
640 SOA (Krechmer et al., 2017). However, an α of 0.1 was an order of magnitude higher than that observed
641 recently for toluene SOA under dry conditions (Zhang et al., 2014). Model results presented hereafter
642 include a kinetic treatment of gas/particle partitioning and assumed an accommodation coefficient of 0.1.

643
644 Results from model simulations performed using different initial condensational sink inputs, some of
645 which captured the influence of new particle formation, are plotted in Figure 3. We found that the initial

Deleted: 10

Deleted: to 100

Deleted: larger

Deleted: 3 to 4

Deleted:

Deleted: VOC

Deleted: nearly identical

Deleted: 0

Deleted: at least to some extent

Deleted: insensitive

Deleted: (factor of ~4

Deleted:) for an α value of 0.01

Deleted: needs t

Deleted: o

Deleted: i

Deleted: of

Deleted: α -pinene

Deleted: (Karnezi et al., 2014)

Deleted:

Deleted: but significantly

666 condensational sink had no influence on the OA predictions from both models for the Idle-Diesel-None
 667 experiment, despite substantial differences in the initial condensational sink between the different cases.
 668 This was because the amount of SOA formed (920 $\mu\text{g m}^{-3}$ at the highest photochemical exposure) was
 669 sufficient to grow the condensational sink enough that the initial condensational sink did not matter. In
 670 contrast, for both models we found large differences between the model predictions of OA for the Idle-
 671 Diesel-DPF+DOC experiment. The use of inputs based on the measurements at no OH exposure, where
 672 the aftertreatment system significantly reduced number concentrations (910 cm^{-3}) and hence the available
 673 condensational sink (0.002 min^{-1}), produced much less SOA (an order of magnitude lower or more) and
 674 poorer agreement with the measurements (see curve (i) in Figure 3(b)). Initial condensational sinks that
 675 captured the influence of new particle formation resulted in higher model predictions but were still about
 676 a factor of ~2 lower for the VBS simulations and a factor of ~2.7 lower for the SOM simulations when
 677 compared against the measurements. The DPF+DOC results also suggest that calculating an initial
 678 condensational sink using data from before and after the photochemical exposure, as done by Palm et al.
 679 (2016), could be used as an input to model OFR data. Slight differences between the different curves for
 680 the Idle-Diesel-None experiment and curves (ii), (iii), and (iv) for the Idle-Diesel-DPF+DOC experiment
 681 can be attributed to the interaction of multigenerational aging and kinetic gas/particle partitioning.

Deleted: 875
 Deleted:

Deleted: 0018
 Deleted: factor of ~3

Deleted: better agreement of the

Deleted: with

683 3.3 Influence of IVOCs on SOA Formation

684 In Figure 4(a), we compare predictions of SOA concentrations from the SOM against measurements for
 685 all the experiments listed in Table 1 and at all photochemical exposures. For visual clarity, we do not
 686 present results from the VBS model as both models had nearly identical predictions with a few
 687 exceptions; see Figure S1 where we compare VBS model predictions to SOM predictions for all
 688 experiments at all photochemical exposures for the base case. The four panels in Figure 4(a) show model-
 689 measurement comparisons assuming four different fractions of IVOCs: 0%, 13.76%, 30%, and 60%;
 690 statistical metrics of fractional bias, fractional error, and R^2 for the comparison for both models are listed
 691 in Table S4 (fractional bias = $\frac{1}{N} \sum_{i=1}^N \frac{M-O}{M+O}$, fractional error = $\frac{1}{N} \sum_{i=1}^N \frac{|M-O|}{M+O}$, M=predicted value,
 692 O=observed value, N=sample size). The model-measurement comparison and the model skill was very
 693 poor when no IVOCs were included (fractional bias = -109%, fractional error = 125%, and $R^2 = 0.52$);
 694 this model reflects the treatment of diesel-powered sources in most traditional emissions inventories and
 695 large-scale models. The model-measurement comparison was reasonable with 13.76% IVOCs (fractional
 696 bias = -46%, fractional error = 101%, and $R^2 = 0.95$) but model predictions were over-predicted with 60%
 697 IVOCs (fractional bias = 72%, fractional error = 97%, and $R^2 = 0.99$). The optimal model performance

Deleted: three
 Deleted: three
 Deleted: .
 Deleted:
 Deleted: 35
 Deleted: 46
 Deleted: 79
 Deleted: performance
 Deleted: improved
 Deleted: 60
 Deleted: 8
 Deleted: 2
 Deleted: and 60% IVOCs
 Deleted: 46
 Deleted: 8
 Deleted: 2

720 that produced the lowest fractional bias and fractional error was realized at an IVOC mass fraction of 30%
721 (fractional bias= 6%, fractional error= 86%, and $R^2 = 0.88$). For predictions with an IVOC mass fraction
722 of 30%, 66% and 70% of the model predictions were within a factor of 1.5 and 2 of the measurements and
723 IVOCs on average accounted for 67%/72% (VBS/SOM) of the SOA at the highest photochemical
724 exposure across all experiments. Given the optimal performance, the base case used in this work assumed
725 a 30% IVOC fraction. These comparisons indicate that it is critical that IVOCs be included when
726 modeling the SOA formation from diesel exhaust and also validate the IVOC composition estimates made
727 by Zhao et al. (2015).

728

729 We further investigated the IVOC species that contributed the most to SOA formation. For an IVOC
730 fraction of 30%, cyclic alkane IVOCs accounted for 23% of the THC emissions and on average accounted
731 for 61%/53% (VBS/SOM) of the SOA formation across the different experiments. We should note that
732 the speciation of cyclic alkane IVOCs in Zhao et al. (2015), while robust in quantifying the carbon
733 number, did not include any specificity in terms of the molecular structure, i.e., their methods would not
734 be able to distinguish between a pure C₁₀ cyclic alkane and a cyclohexane with a 4-carbon branch.
735 Further, the parameterizations to model SOA formation from cyclic alkane IVOCs for both models were
736 based on the behavior of particular compounds. In the VBS model when using the high NO_x
737 parameterizations, the surrogate for a cyclic alkane IVOC was determined through equivalence with a
738 straight alkane IVOC while in the VBS model when using the low NO_x parameterizations or the SOM the
739 cyclic alkane IVOCs were tied to parameterizations for hexylcyclohexane. (The observed SOA yield and
740 derived SOM parameterization for hexylcyclohexane is actually quite similar to that for cyclododecane
741 for low-NO_x conditions, but not for high-NO_x conditions (Cappa et al., 2013)) This lack of specificity in
742 the speciation and the SOA parameterizations made the SOA predictions from the oxidation of cyclic
743 alkane IVOCs relatively uncertain. To examine the sensitivity of the model predictions to uncertainties in
744 the model treatment of cyclic alkane IVOCs, we performed simulations with both models for one of the
745 Idle-Diesel-None experiments where the cyclic alkane IVOCs were treated as branched alkane IVOCs;
746 results from these simulations are shown in Figure 5(a). The use of branched alkane IVOCs to model
747 cyclic alkane IVOCs only marginally reduced OA predictions for both the VBS and SOM models,
748 suggesting that the model predictions were not sensitive to the SOA parameterization used for cyclic
749 alkane IVOCs. Regardless, we recommend that future work focus on a more detailed speciation of cyclic
750 alkane IVOCs in combustion emissions as well as on chamber and OFR experiments on those speciated
751 compounds to improve quantification of their SOA mass yields.

- Deleted: 40
- Deleted: -10
- Deleted: X
- Deleted: 97
- Deleted: X
- Deleted: 0.9
- Deleted: X
- Deleted: (not shown)
- Deleted: 4
- Deleted: 59
- Deleted: X
- Deleted: 68
- Deleted: Y
- Deleted: X
- Deleted: Y
- Deleted: .
- Deleted:
- Deleted: emissions and
- Deleted: for IVOCs
- Deleted: - [1]
- Deleted: C
- Deleted: 45
- Deleted: contributed
- Comment [SE3]: Calculated for all experiments (0.5v to 4v) for SOM & VBS
- Deleted: X
- Deleted: Y
- Deleted: 40 10 to 84
- Deleted: 75
- Deleted:
- Deleted: NO_x
- Deleted: NO_x
- Deleted: .
- Deleted: at the highest photochemical exposure by 33% and 11%
- Deleted: respectively
- Deleted: modestly
- Deleted: W

790 As there were no direct measurements of any SOA precursors in the study of [Jathar et al. \(2017a\)](#), we
791 have used previously published emissions profiles for diesel exhaust to determine initial concentrations of
792 the SOA precursors. We examined the sensitivity of model predictions to two different emissions profiles
793 from the EPA SPECIATE (version 4.3) database: Profile #3161 (included in the base case) and Profile
794 #8774 that represents emissions from ‘Heavy Duty Diesel Exhaust’; the speciation for both profiles is
795 provided in Tables S2 and S3. Both profiles only included speciation for VOC emissions and in these
796 simulations we assumed an IVOC mass fraction of 30%. The results captured in Figure 5(b) for one of the
797 Idle-Diesel-None experiments show that the choice in the emissions profile had no influence on the OA
798 evolution for the VBS model but had a small influence on the OA evolution for the SOM. This little to
799 small influence was expected given that most of the SOA was formed from IVOC, rather than VOC,
800 oxidation. This further demonstrates that IVOCs, not VOCs, play an important role in controlling the
801 SOA formation from diesel exhaust emissions and it is important that future studies work towards better
802 understanding the IVOC speciation.

803
804 The IVOC speciation of [Zhao et al. \(2015\)](#) included 37 unique species, each of which required a unique
805 surrogate to model the SOA formation from that species. Tracking these many IVOC species in an
806 atmospheric model (e.g., global climate model) may be intractable and hence, there is a need to develop
807 simplified parameterizations to efficiently model SOA formation from IVOCs. We note that species using
808 the same surrogate in the VBS model (e.g., a C₁₅ linear alkane, C₁₇ branched alkane, and C₁₃ cyclic alkane
809 are all parameterized using *n*-pentadecane when using the high NO_x parameterizations) could be lumped
810 together to reduce the number of precursors and products tracked and that there are no penalties for a
811 precursor type (e.g., *n*-alkanes) to include additional precursor and product species once a SOM grid is
812 setup. Nonetheless, to investigate the possibility of developing a simplified parameterization, we modeled
813 SOA from IVOCs assuming that all the IVOCs could be modeled together as a single linear C₁₃, C₁₅, C₁₇
814 or C₁₉ alkane; a similar strategy was employed by ([Jathar et al., 2014b](#)) to model SOA formation from
815 unspciated organic compounds in combustion emissions. Results from these simulations are shown in
816 Figure 5(c) for one of the Idle-Diesel-None experiments. For the VBS model, the use of a larger carbon
817 number alkane to model IVOC SOA produced increasingly more OA, with the C₁₉ alkane providing the
818 best comparison against measurements. For the SOM, the use of a C₁₃ and C₁₅ alkane produced good
819 agreement with measurements with a C₁₃ alkane slightly under-predicting the OA at 0.5 OH days and the
820 C₁₅ alkane slightly over-predicting the OA at lower photochemical exposures (0.06 and 0.17 OH days). It
821 was interesting to observe that for the SOM, in contrast to the VBS, the use of different linear alkanes
822 produced different OA masses at lower photochemical exposures but converged at the highest

Deleted: 1

Deleted: 2

Deleted: 6

Deleted: very little

Deleted: , which

Deleted: or

Deleted: the use of a linear C₁₅ and C₁₇ alkane parameterization for IVOCs reproduced the measurements well.

Deleted: a

Deleted: linear

Deleted: C₁₇

Deleted: parameterizations

836 photochemical exposure suggesting that the effective SOA mass yield in the SOM varied dynamically
837 with photochemical age. Differences in the VBS and SOM predictions with different alkane
838 parameterizations point to inherent differences in the coupled representation of multigenerational aging
839 and gas/particle partitioning. Results from these simulations indicate that in cases where computational
840 efficiency is demanded, the SOA formation from IVOCs in diesel exhaust could be modeled using a
841 surrogate linear alkane, possibly a C₁₃ linear alkane with the VBS and a C₁₃ or C₁₅ linear alkane for the
842 SOM.

Deleted:
Deleted:
Deleted: 5
Deleted: or a
Deleted: 7
Deleted: .

844 3.4 Elemental Composition

845 The SOM tracks both the carbon and oxygen number of the oxidation products, which allowed us to
846 predict the O:C ratio of the OA. The O:C of the OA was calculated by combining the measured O:C of
847 the POA with the modeled O:C of the SOA. We compare predictions of the O:C of OA from the SOM
848 against measurements for all the experiments listed in Table 1 and at all photochemical exposures in
849 Figure 4; statistical metrics of fractional bias, fractional error, and R^2 for the comparison are listed in
850 Table S5. Model predictions for the no IVOC case, where the O:C of the OA was dominated by the O:C
851 of the aromatic SOA, compared well with measurements (fractional bias = -4.2%, fractional error = 28%,
852 and $R^2 = 0.77$). However, the poor OA mass predictions with no IVOCs suggests that the good O:C
853 performance was purely coincidental. The 13.76%, 30%, and 60% IVOC cases under-predicted the OA
854 O:C where the under-prediction appeared to increase as the IVOC influence increased; fractional bias = -
855 32%, fractional error = 38%, and $R^2 = 0.72$ for the 13.76% IVOC case, fractional bias = -37%, fractional
856 error = 42%, and $R^2 = 0.70$ for the 30% IVOC case, and fractional bias = -60%, fractional error = -62%,
857 and $R^2 = 0.46$ for the 60% IVOC case. A higher IVOC fraction resulted in a lower O:C ratio because the
858 IVOCs were primarily composed of higher carbon number species that on oxidation produced low O:C
859 SOA compared to SOA formed from precursors such as aromatics. On average, the 30% IVOC case
860 predicted an O:C ratio that was a factor of 1.5 lower than the measurements. For the three non-zero IVOC
861 cases (13.76%, 30%, and 60%), the model skill in predicting the O:C was much better for the non-
862 DPF+DOC experiments ($R^2 = 0.82$, 0.83, and 0.80 respectively) than for the DPF+DOC experiments (R^2
863 = 0.02, 0.02, and 0.29 respectively). Measurements and model predictions of the OA O:C ratio from the
864 30% IVOC case as a function of photochemical age are presented in Figure S2.

Deleted: 3
Deleted: 9
Deleted: 80
Deleted: Both t
Deleted: 41
Deleted: 43
Deleted: 5
Deleted: 55
Deleted: 57
Deleted: 49
Deleted: 55
Deleted: 57
Deleted: 9
Deleted: ,
Deleted: o
Deleted: X
Deleted: by about a factor of two although the 13.76%
IVOC case offered a slightly better model performance than
the 60% IVOC case (fractional bias = -41%, fractional error
= 43%, and $R^2 = 0.75$ for the 13.76% IVOC case versus
fractional bias = -55%, fractional error = 57%, and $R^2 = 0.49$
for the 60% IVOC case).
Deleted: both the 13.76% and 60%
Deleted: 3
Deleted: X
Deleted: 5
Deleted: X
Deleted: 0% and 6

865
866 The under-prediction in O:C ratios was confounding when compared to earlier applications of the SOM
867 and in light of the reasonable model-measurement comparison found in this work in predicting OA mass.
868 We note that the low O:C in the 13.76%, 30%, and 60% IVOC cases stems from the dominance of

903 product species that have high carbon numbers and low oxygen numbers. We explored several lines of
904 reasoning for this under-prediction. First, [Cappa et al. \(2013\)](#) found good agreement between the SOM-
905 predicted and observed O:C for chamber experiments conducted using individual linear, branched and
906 cyclic C₁₂ alkanes. Also, general predictions of the dependence of O:C on the carbon number of the parent
907 hydrocarbon (cf. Fig. 2b in [Cappa and Wilson \(2012\)](#)) show good agreement with observations (cf. Fig.
908 2a in [Tkacik et al. \(2012\)](#)), both in terms of absolute values and shape. This suggests that uncertainties in
909 the SOM parameters may not be the dominant reason for the under-prediction. A possible reason for the
910 under-prediction then is that the compounds identified by [Zhao et al. \(2015\)](#) as IVOCs are structurally
911 different than the alkanes used to model them in this work. **Second**, the gas-phase chemistry in the OFR
912 might be inherently different than that in a chamber. For example, kinetic limitations to gas/particle
913 partitioning may result in gas-phase oxidation of low-volatility products having high O:C that typically
914 would have partitioned to the particle phase in a chamber experiment but instead are fragmented ([Palm et
915 al., 2016](#)). As to why the chamber-based SOM parameters then offer good model performance on OA
916 mass remains unclear. One way in which this issue could be addressed in the future is by developing
917 SOM parameters exclusively based on OFR data, as and when they become available. **Third**, the SOM
918 used here did not include surface/heterogeneous and particle-phase reactions that might influence the OA
919 composition and O:C ratio. When heterogeneous reactions of OA were included assuming an OH uptake
920 coefficient of 1 (the product distribution from the oxidation reaction was kept the same as the gas-phase
921 reactions), SOA production at the highest photochemical exposure for all the experiments was reduced, on
922 average, by 7% from fragmentation reactions within the particle phase, but the O:C ratio was only
923 marginally increased (average of 2%).

924
925 To understand the O:C under-prediction better, we compared model predictions of normalized gas-phase
926 species concentrations from the SOM to normalized gas-phase measurements made by [Friedman et al.
927 \(2017\)](#) using a chemical ionization mass spectrometer (CIMS). The CIMS detects an array of oxygenated
928 organic species and the high resolution of the time-of-flight mass spectrometer enables identification of
929 the elemental composition of each detected peak. The CIMS data were aggregated by carbon and oxygen
930 number to facilitate comparison with the SOM data. The comparison was performed on a normalized
931 basis because the CIMS did not provide absolute concentrations for every detected peak. The SOM-CIMS
932 comparisons for the Idle-Diesel-None and Load-Diesel-None experiments at the highest photochemical
933 exposure are shown in Figure 6, which highlight four findings of note. First, the CIMS measured species
934 larger than a carbon number of 12 that are presumably products from oxidation of higher molecular
935 weight organic compounds, although the possibility of dimer formation in the instrument cannot be

Deleted: Second, it is possible that we incorrectly assumed, based on the measured VOC:NO_x ratio (1.9 and 4.1 ppbC ppbN⁻¹ for the Idle experiments and 0.06–0.55 ppbC ppbN⁻¹ for the Load experiments), that the SOA was formed under high NO_x conditions and that we would need to use SOM parameters developed from high NO_x experiments. In an OFR, high oxidant loadings (OH and O₃) could rapidly reduce NO_x at the OFR inlet and result in most of the SOA being formed at low NO_x conditions (Peng and Jimenez, 2017). We performed simulations to examine the sensitivity of model predictions to the use of SOM parameters developed from low NO_x experiments. We found that the SOM resulted in an average increase of only 5% in O:C predictions but an average increase of 65% in OA mass across all experiments at the highest photochemical exposure. A better understanding of the NO_x chemistry inside the OFR (Peng and Jimenez, 2017) might provide insight on the parameterizations needed to model SOA formation in OFRs. Third

Deleted: And finally

Deleted: 10

Deleted: 1

Deleted: three

959 entirely ruled out. Nonetheless, this provides additional evidence for the presence of IVOC oxidation
960 products in diesel exhaust emissions. Second, the CIMS measured organic compounds with high O:C
961 ratios (e.g., C₆O₆, C₇O₇). This implies that the reaction chemistry in OFRs rapidly adds functional groups
962 to the carbon backbone, although larger, less oxidized compounds could be simultaneously functionalized
963 and fragmented in the CIMS leading to the appearance of highly oxidized species. Third, the SOM offered
964 a reasonable correlation against the CIMS measurements for both experiments across a majority of the
965 carbon-oxygen combinations that spanned more than four orders of magnitude. Qualitatively, this finding
966 validates the statistical evolution of organic compounds tracked through the generalized SOM
967 mechanism, although certainly some differences are evident. Finally, for the mid-carbon number species
968 (~C₁₀), the SOM seemed to produce higher fractions of species with low oxygen numbers (O₀ to O₃) but
969 lower fractions of species with high oxygen numbers (O₅ to O₇). This under-prediction of the high oxygen
970 number species might potentially explain why the SOM may be under-predicting the OA O:C ratio. The
971 SOM-CIMS comparison is preliminary and we intend to explore the implications of this comparison in
972 future work.

973

974 3.5 Other Model Sensitivities

975 We performed sensitivity analyses to examine the influence of other key processes on predictions from
976 both the VBS and SOM models. When examining the sensitivity to each process, all the other inputs were
977 kept the same as those listed in the base case. We only present sensitivity results for the Idle-Diesel-None
978 experiment performed on June 5, as the results for this experiment were generally representative of all
979 experiments (Figure 7). For completeness, we performed simulations for all the experiments at the highest
980 photochemical exposure since each of the processes explored below manifested the strongest response at
981 the highest photochemical exposure. The results from these simulations are presented as a change in the
982 model predictions relative to that offered by the base case.

983

984 **Multi-generational Aging.** One of the key differences between the VBS and the SOM models is how they
985 represent the multi-generational aging of gas-phase products. SOA parameters for the VBS model
986 represent stable product distributions at the end of the chamber experiments and therefore already include
987 the influence of multi-generational aging reactions encountered during the chamber experiment.
988 Additional multi-generational aging in the VBS model, based on the scheme of [Robinson et al. \(2007\)](#), is
989 simulated as a continuous decrease in product volatility, which does not account for fragmentation
990 reactions and has not been constrained against experiments. The SOM framework explicitly models multi-
991 generational aging that includes treatment of fragmentation reactions and constrains the aging reactions

Deleted: to lead

Deleted: having only 6 carbon atoms

Deleted: compared to the Idle-Diesel-None experiment, the SOM over-predicted the fractional contribution of low-oxygen number species (O₀ to O₃, factor of 5) and under-predicted some of the high oxygen number species (O₅ to O₇, factor of 2) in the Load-Diesel-None experiment.

999 based on the chamber experiments to an extent that is determined by the length (in OH exposure space) of
000 the experiment. To test the influence of multi-generational aging, we performed model simulations with
001 aging turned off for the VBS and SOM models and plot the results in Figure 7(a). We found that aging
002 had a small influence (~18% reduction in OA mass) on model predictions from the VBS model, most
003 likely because the high SOA and OA mass concentrations resulted in a substantial fraction of the organic
004 species to be partitioned to the particle phase. This left very little of the organic species in the gas-phase to
005 participate in multi-generational aging. We calculated that less than 20% by mass of the product species
006 in this experiment was in the gas-phase at the OA mass concentration at the highest photochemical
007 exposure, implying that the SOA mass yields at these OA mass concentrations were rapidly approaching
008 100%. In contrast, the absence of aging resulted in a 43% decrease in the OA mass for the SOM. The
009 decrease was mainly because the first generation oxidation product with the highest yield (i.e., C_xO₁) was
010 too volatile to partition to the particle phase and needed to be aged further to form condensable products.
011 As noted earlier, the term aging is defined differently for the VBS and SOM models and the results
012 presented here need to take the definitional issues into account when examining the influence of aging.
013 Compared to the base case, no aging resulted in an average decrease of 4% and 30% in OA mass for the
014 VBS and SOM models respectively for all experiments at the highest photochemical exposure. These
015 simulations suggest that aging of the oxidation products, at least for the SOM, is as important as the
016 contribution of first generation products to SOA formation.

017
018 **Vapor Wall Losses.** Prior work has highlighted the influence vapor wall losses exert on the calculation of
019 SOA mass yields from chamber experiments (Zhang et al., 2014; Krechmer et al., 2016). Cappa et al.
020 (2016), based on the chamber work of Zhang et al. (2014), recently published parameter sets for the SOM
021 that accounted for no vapor wall losses and two different vapor wall loss rates (1×10^{-4} and 2.5×10^{-4} s⁻¹)
022 assuming an equivalent OA mass of the chamber walls of 10 mg m⁻³ (the base case used the parameter
023 sets for a vapor wall loss rate of 2.5×10^{-4} s⁻¹). We performed model simulations with SOM using
024 parameters that were either not corrected for vapor wall losses or that were corrected for vapor wall losses
025 using either the low (1×10^{-4}) or high (2.5×10^{-4}) estimates proposed by Cappa et al. (2016). The results
026 plotted in Figure 7(b) show that correcting for vapor wall losses significantly increased model predicted
027 OA mass (by 73% and 112% for the low wall loss and high wall loss cases respectively at the highest
028 photochemical exposure when compared to the no wall loss case) and provided the best performance for
029 the high estimate for vapor wall losses. Across all experiments and at the highest photochemical exposure,
030 accounting for vapor wall losses using the high estimate resulted in an average increase of 39% over no
031 accounting for vapor wall losses. These comparisons suggest that it is important to use SOA

Deleted: no
Deleted: 20

Deleted: ; w
Deleted: 1

Deleted: approached

Deleted: 6

Deleted: <
Deleted: 1
Deleted: 27

Deleted: slightly

Deleted: 42

Deleted: 8

Deleted: 53

Deleted: 27

Comment [Office4]: Sailaja: seems low compared to our finding in Figure 7(b).

Deleted: 36

047 parameterizations in which vapor wall losses in chambers have been accounted for when interpreting
048 SOA experiments. Furthermore, we also simulated the influence of vapor losses to the OFR walls on
049 model predictions. We assumed reversible uptake of vapors to the walls and used a vapor wall loss rate of
050 $2.5 \times 10^{-3} \text{ s}^{-1}$ (factor of ~ 10 larger than that for a chamber) based on the work of [Palm et al. \(2016\)](#) and an
051 equivalent OA mass concentration of 10 mg m^{-3} for the OFR walls. The results plotted in Figure 7(b)
052 show that the loss of vapors to the OFR walls had a small influence on model predictions: a 6.5%
053 decrease for this experiment and an average decrease of 11% across all experiments at the highest
054 photochemical exposure. Increasing the equivalent OA mass concentration for the OFR walls to 100 and
055 1000 mg m^{-3} seemed to have no influence on model predictions. These findings imply that vapor wall
056 losses in the presence of sufficient seed aerosol might not be of concern for OFRs ([Lambe et al., 2015](#)).

Deleted: 9
Deleted: 2

058 **Residence Time Distributions.** Model simulations performed in this work assumed that the OFR operated
059 as a plug flow reactor with a constant residence time. Experimental studies by [Lambe et al. \(2011\)](#) and
060 fluid dynamics simulations by [Ortega et al. \(2016\)](#) have shown that OFRs, particularly like the one used
061 in this work, exhibit heterogeneity in residence times. We performed simulations to explore the sensitivity
062 of varying residence times on model predictions. These simulations were performed based on a
063 discretized version of the residence time distribution measured by [Lambe et al. \(2011\)](#) for SO_2 that
064 yielded an average residence time of 100 seconds (same as that used by [Jathar et al. \(2017a\)](#)). The
065 discretized version included six parcels with volume fractions of 0.23, 0.36, 0.24, 0.11, 0.05, and 0.01
066 with residence times of 45, 65, 100, 200, 300, and 500 seconds respectively. Each parcel experienced the
067 same OH concentration but the varying residence times resulted in different OH exposures for each
068 parcel. The parcels were combined after photochemical exposure without repartitioning the OA between
069 the six parcels. Similar to the findings of [Peng et al. \(2015\)](#) for calculating OH exposure, our results in
070 Figure 7(c) show that using a residence time distribution had very little influence on the OA mass
071 evolution compared to use of an effective average time. Compared to the base case, the residence time
072 distribution resulted in an average decrease of 3% and 5% in OA mass for the VBS and SOM models
073 respectively for all experiments at the highest photochemical exposure.

Deleted: X
Deleted: 3
Deleted: Y
Deleted: 7

075 **Spatial Heterogeneity in OH.** In addition to the influence exerted by a distribution of residence times,
076 spatial heterogeneity in the gas-phase chemistry inside the OFR (e.g., from radial variation in light
077 intensity) could lead to spatial heterogeneity in OH concentrations and result in a distribution of OH
078 exposures for the sample being aged. We performed simulations to explore the sensitivity of a varying
079 OH exposure on model predictions. These simulations were performed where we split the sample coming

086 into the OFR into two parcels and treated the parcels to different OH exposures. Each experiment was
087 repeated for all combinations (six total) of three different parcel splits ($\frac{1}{4}$ - $\frac{3}{4}$, $\frac{1}{3}$ - $\frac{2}{3}$, $\frac{1}{2}$ - $\frac{1}{2}$) and two different
088 OH exposure splits ($\frac{1}{3}$ -X, $\frac{2}{3}$ -X); X was determined by conserving the total OH exposure reported by
089 [Jathar et al. \(2017a\)](#). For instance, the first simulation was performed by splitting the OFR air parcel into
090 $\frac{1}{4}$ and $\frac{3}{4}$ fractions by volume and exposing the $\frac{1}{4}$ volume to $\frac{1}{3}$ the OH exposure. The parcels were
091 combined after photochemical exposure without repartitioning the OA between the two parcels. The
092 results in Figure 7(d) show that the simulated spatial heterogeneity always reduced the OA mass although
093 the maximum reduction (13% for the VBS and 14% for the SOM models) at the highest photochemical
094 exposure was within the measurement uncertainty at least for the SOM. Compared to the base case, the
095 spatial heterogeneity in OH resulted in a maximum decrease of 13% and 15% in OA mass for the VBS
096 and SOM models respectively for all experiments at the highest photochemical exposure.

Deleted: 2
Deleted: 5
Deleted: well
Deleted: 2
Deleted: 14

097 4. Summary and Discussion

098 Recently, [Jathar et al. \(2017a\)](#) reported on experiments performed using the oxidation flow reactor (OFR)
099 to measure the photochemical production of secondary organic aerosol (SOA) from diesel exhaust under
100 varying engine loads, fuel types, and [aftertreatment](#) systems. These data present an opportunity to not only
101 test SOA models but also use these models to interpret OFR data and determine their relevance for the
102 real atmosphere. In this work, we applied two different SOA model frameworks (VBS and SOM) to
103 simulate the photochemical production of SOA in an OFR from diesel exhaust and evaluated those model
104 frameworks using the data from [Jathar et al. \(2017a\)](#). The volatility basis set (VBS) model is a
105 parameterized model that allows for a volatility-based representation of OA while the statistical oxidation
106 model (SOM) is a semi-explicit parameterized model that uses a carbon-oxygen grid to track OA. Both
107 simulated the coupled chemistry, thermodynamic properties, and gas/particle partitioning of OA and
108 accounted for: (i) semi-volatile and reactive emissions of primary organic aerosol (POA), (ii) SOA
109 production from IVOCs and VOCs, (iii) multi-generational aging, and (iv) kinetic gas/particle
110 partitioning.
111

Deleted: emissions control

112
113 Model predictions suggest that the instantaneous gas/particle partitioning assumption may over-predict
114 SOA formation in OFRs when the initial condensational sinks are low and the condensation of SOA is
115 likely kinetically limited. Hence, SOA formation in OFRs needs to be modeled/interpreted through an
116 explicit treatment of kinetic gas/particle partitioning. Differences in model predictions between
117 instantaneous and kinetic partitioning will depend on the rate at which condensable SOA mass is
118 produced in the OFR (depends on the initial precursor concentrations and photochemical exposure),

125 residence time in the OFR, properties of the condensing species (e.g., diffusion coefficient, molecular
126 weight), and parameters relevant for partitioning (e.g., accommodation coefficient, seed aerosol surface
127 area). To explore the relative importance of instantaneous and kinetically-limited partitioning in an OFR,
128 we used the SOM to simulate SOA formation from diluted diesel exhaust using instantaneous and kinetic
129 partitioning assumptions for varying amounts of SOA formed ($1-10000 \mu\text{g m}^{-3}$) and initial condensational
130 sinks ($0.001-10 \text{ min}^{-1}$). These simulations were similar to the calculations performed by Palm et al. (2017)
131 where they calculated timescales and losses of condensable SOA vapors to the OFR walls and sampling
132 lines and reaction with OH. The calculations were performed for two different initial particle sizes (10
133 and 100 nm) since the condensation of SOA mass would grow the initial condensational sink for the two
134 particles at different rates, i.e. for the same starting initial condensational sink, smaller particles would
135 experience quicker growth in the condensational sink compared to larger particles for the same amount of
136 condensing mass. The calculations were also performed for two different residence times – 2 and 4
137 minutes – to span the residence time range used in typical applications of the OFR. We assumed an
138 accommodation coefficient of 0.1. The results plotted in Figure 8 show the ratio of SOA predicted
139 through kinetic partitioning to that predicted through instantaneous partitioning as a function of the initial
140 condensational sink and the SOA formed under an instantaneous partitioning assumption. Across the four
141 scenarios explored (two initial particle sizes and two residence times), the SOA formation predicted under
142 the kinetic partitioning assumption was an order of magnitude or more lower than that predicted under the
143 instantaneous partitioning assumption over a large portion of the input range explored, e.g., when the
144 initial condensational sink was smaller than $\sim 0.1 \text{ min}^{-1}$ and the maximum SOA formed was lower than
145 $\sim 100 \mu\text{g m}^{-3}$ for the 10 nm simulations and lower than $\sim 1000 \mu\text{g m}^{-3}$ for the 100 nm simulations. We also
146 found that the SOA formation in the OFR was kinetically-limited under typical ambient conditions. The
147 SOA formation predicted under the kinetic partitioning assumption approached the SOA formed under the
148 instantaneous partitioning assumption either when the initial condensational sink was very large ($>5 \text{ min}^{-1}$
149 1) or when a large amount of condensable SOA was produced in the OFR ($\geq 1000 \mu\text{g m}^{-3}$ for the 10 nm
150 particles and $\gg 10000 \mu\text{g m}^{-3}$ for the 100 nm particles). Our finding implies that ambient applications of
151 the OFR, where initial condensational sinks are typically smaller ($\sim 0.005-0.5 \text{ min}^{-1}$) and the maximum
152 SOA produced is typically less than $40 \mu\text{g m}^{-3}$, will only produce a small fraction (0-30%) of the intended
153 SOA. Furthermore, our simulations suggested that a smaller initial particle size (i.e., 10 nm) for the same
154 initial condensational sink and a longer OFR residence time (i.e., 4 min) may not necessarily help produce
155 the intended SOA under ambient conditions. Although these simulation results need to be verified
156 experimentally, they do suggest that it might be challenging to operate the OFR in conditions where
157 instantaneous or atmospherically-relevant partitioning is applicable, further complicating the coupled

Deleted: 0.

Deleted:

Deleted: We assumed a

Deleted: in the OFR of

Deleted: 100 s and an

Deleted: Increasing the OFR residence time to 240 s and accommodation coefficient to 1.0 did not dramatically alter the findings and hence have not been considered in this work.

Deleted: 1

Deleted: 1

Deleted: 1

Deleted: In other words, wWe

Deleted: over most a large portion of the input ranges explored

Deleted: and

Deleted: 20

Deleted: 1

Deleted: 0

177 atmospheric simulation of chemistry and thermodynamics in OFRs.

178

179 Upon including IVOCs as SOA precursors, both the VBS and SOM models were able to reasonably
180 predict the OA mass evolution reported by [Jathar et al. \(2017a\)](#) across different engine loads, fuel types,
181 and [aftertreatment](#) systems. Model predictions suggest that 30% of the unburned hydrocarbon emissions
182 are likely IVOCs and that these IVOCs (regardless of the emissions profiles used to determine non-IVOC
183 emissions), account for most (average of 70%) of the SOA formed from diesel exhaust. These findings are
184 consistent with prior work from chamber experiments ([Jathar et al., 2014b](#)) and modeling studies ([Zhao et
al., 2015](#)). Simulations performed using single surrogates suggest that the complex mixture of IVOCs in
186 diesel exhaust could be well represented using a linear C₁₃ or C₁₅ alkane for the SOM but might need a
187 larger surrogate such as a C₁₉ alkane for the VBS model. The need for a different surrogate species to
188 model IVOC SOA between the SOM and VBS models most likely arises from differences in the coupled
189 treatment of the oxidation chemistry and gas/particle partitioning in the OFR. The use of surrogates offers
190 a computationally-efficient strategy to model SOA formation from IVOCs in large-scale three-
191 dimensional models. The SOM tracks the carbon and oxygen numbers of the oxidation products and
192 hence model predictions were used to calculate atomic O:C ratios for OA, which were then compared to
193 measurements. While the inclusion of IVOCs allowed for good model-measurement comparisons on OA
194 mass, the SOM under-predicted the O:C ratio of OA by a factor of 1.5, possibly highlighting the
195 limitations in modeling the IVOCs as alkanes and/or extrapolating chamber-based parameterizations to
196 OFR experiments. Model predictions of the gas-phase organic species compared favorably to those
197 measured using a chemical ionization mass spectrometer (CIMS), which qualitatively validates the
198 statistical evolution of organic compounds tracked through the generalized SOM mechanism.

199

200 As OFRs are increasingly used to study SOA formation and evolution in laboratory and field
201 environments, there is a need to develop models that can be used to interpret OFR data. This work
202 suggests that multi-generational aging (in case of the VBS model), residence time distributions, and
203 spatial heterogeneity in OH concentrations produced sensitivities that were well within the measurement
204 uncertainty and were not a concern for the model system studied. However, model predictions did appear
205 to be more sensitive to multi-generational aging (in case of the SOM) and influence of vapor wall losses,
206 highlighting that these processes be included in OFR models. While the conclusions from this work may
207 be relevant for other laboratory and ambient studies, their relative importance may vary. There are several
208 instances where the model development was insufficient and will likely be addressed in future work. For
209 example, the model could benefit from the use of a polydisperse size distribution to treat new particle

Deleted: emissions control

Deleted: 4

Deleted: would

Deleted: >

Deleted: 90

Deleted: 57

Deleted: X

Deleted: 5

Deleted: 7

Deleted: These

Deleted: slightly less than a

Deleted: two

222 formation and growth and improve predictions of the evolution of the aerosol size distribution. Similarly,
223 the model needs to be rigorously tested against other laboratory (e.g., [Lambe et al. \(2012\)](#)) and ambient
224 (e.g., [Palm et al. \(2016\)](#)) OFR data.

225

226 **5 Acknowledgements**

227 [We thank Dr. Zhe Peng and Dr. Jose Jimenez for running their oxidation flow reactor model \(Peng and](#)
228 [Jimenez, 2017\) to provide NO_x relevant inputs for our work.](#) We thank the Dr. Jeffrey Pierce and Dr.
229 John Volckens for their feedback on the written manuscript. DKF acknowledges the Beckman Young
230 Investigator Award for funding.

231

232 **6 References**

- 233 Ahlberg, E., Falk, J., Eriksson, A., Holst, T., Brune, W. H., Kristensson, A., Roldin, P., and Svenningsson, B.:
234 Secondary organic aerosol from VOC mixtures in an oxidation flow reactor, *Atmospheric environment*, 161, 210-220, 2017.
- 235 Ahmadov, R., McKeen, S. A., Robinson, A. L., Bahreini, R., Middlebrook, A. M., de Gouw, J. A., Meagher, J., Hsie,
236 E. Y., Edgerton, E., Shaw, S., and Trainer, M.: A volatility basis set model for summertime secondary organic aerosols over
237 the eastern United States in 2006, *Journal Of Geophysical Research-Atmospheres*, 117, D06301, 2012.
- 238 Anderson, J. O., Thundiyil, J. G., and Stolbach, A.: Clearing the air: a review of the effects of particulate matter air
239 pollution on human health, *Journal of Medical Toxicology*, 8, 166-175, 2012.
- 240 Atkinson, R., and Arey, J.: Atmospheric degradation of volatile organic compounds, *Chemical Reviews*, 103, 4605-
241 4638, 2003.
- 242 Bond, T., Venkataraman, C., and Masera, O.: Global atmospheric impacts of residential fuels, *Energy for Sustainable*
243 *Development*, 8, 20-32, 2004.
- 244 Cappa, C., and Wilson, K.: Multi-generation gas-phase oxidation, equilibrium partitioning, and the formation and
245 evolution of secondary organic aerosol, *Atmospheric Chemistry and Physics*, 12, 9505-9528, 2012.
- 246 Cappa, C. D., Zhang, X., Loza, C. L., Craven, J. S., Yee, L. D., and Seinfeld, J. H.: Application of the Statistical
247 Oxidation Model (SOM) to Secondary Organic Aerosol formation from photooxidation of C 12 alkanes, *Atmospheric*
248 *Chemistry and Physics*, 13, 1591-1606, 2013.
- 249 Cappa, C. D., Jathar, S. H., Wexler, A. S., Seinfeld, J., and Kleeman, M. J.: Simulating secondary organic aerosol in a
250 regional air quality model using the statistical oxidation model – Part 2: Assessing the influence of vapor wall losses,
251 *Atmospheric Chemistry & Physics*, 16, 3041-3059, 2016.
- 252 Chacon-Madrid, H., and Donahue, N.: Fragmentation vs. functionalization: chemical aging and organic aerosol
253 formation, *Atmos. Chem. Phys*, 11, 10553-10563, doi:10.5194/acp-11-10553-2011 2011.
- 254 Chan, A. W. H., Kautzman, K. E., Chhabra, P. S., Surratt, J. D., Chan, M. N., Crounse, J. D., Kurten, A., Wennberg,
255 P. O., Flagan, R., and Seinfeld, J. H.: Secondary organic aerosol formation from photooxidation of naphthalene and
256 alkylnaphthalenes: implications for oxidation of intermediate volatility organic compounds (IVOCs), *Atmospheric Chemistry*
257 *and Physics*, 9, 3049-3060, 2009.
- 258 Chen, S., Brune, W., Lambe, A., Davidovits, P., and Onasch, T.: Modeling organic aerosol from the oxidation of

259 alpha-pinene in a Potential Aerosol Mass (PAM) chamber, *Atmospheric Chemistry and Physics*, 13, 5017-5031, 2013.

260 Chirico, R., DeCarlo, P., Hering, M., Tritscher, T., Richter, R., Prevot, A., Dommen, J., Weingartner, E., and Wehrle,
261 G.: Impact of aftertreatment devices on primary emissions and secondary organic aerosol formation potential from in-use
262 diesel vehicles: results from smog chamber experiments, *Atmospheric Chemistry and Physics*, 10, 11545-11563, 2010.

263 Donahue, N., Robinson, A., Stanier, C., and Pandis, S.: Coupled partitioning, dilution, and chemical aging of
264 semivolatile organics, *Environ. Sci. Technol.*, 40, 2635-2643, doi:10.1021/es052297c, 2006a.

265 Donahue, N., Epstein, S., Pandis, S., and Robinson, A.: A two-dimensional volatility basis set: 1. organic-aerosol
266 mixing thermodynamics, *Atmospheric Chemistry and Physics*, 11, 3303-3318, 2011.

267 Donahue, N. M., Robinson, A. L., Stanier, C. O., and Pandis, S. N.: Coupled partitioning, dilution, and chemical aging
268 of semivolatile organics., *Environ. Sci. Technol.*, 40, 2635-2643, 2006b.

269 Dzepina, K., Volkamer, R., Madronich, S., Tulet, P., Ulbrich, I., Zhang, Q., Cappa, C., Ziemann, P., and Jimenez, J.:
270 Evaluation of recently-proposed secondary organic aerosol models for a case study in Mexico City, *Atmospheric Chemistry
271 and Physics*, 9, 5681-5709, doi:10.5194/acp-9-5681-2009, 2009.

272 Ensberg, J. J., Hayes, P. L., Jimenez, J. L., Gilman, J. B., Kuster, W. C., de Gouw, J. A., Holloway, J. S., Gordon, T.
273 D., Jathar, S., and Robinson, A. L.: Emission factor ratios, SOA mass yields, and the impact of vehicular emissions on SOA
274 formation, *Atmospheric Chemistry and Physics*, 14, 2383-2397, 2014.

275 EPA: SPECIATE Version 4.3, in, 2013.

276 EPA: Estimation Programs Interface Suite™, in, United States Environmental Protection Agency, Washington, DC,
277 USA., 2017.

278 Friedman, B., Brophy, P., Brune, W. H., and Farmer, D. K.: Anthropogenic Sulfur Perturbations on Biogenic
279 Oxidation: SO₂ Additions Impact Gas-Phase OH Oxidation Products of α - and β -Pinene, *Environ. Sci. Technol.*, 50, 1269-
280 1279, 10.1021/acs.est.5b05010, 2016.

281 Friedman, B., Link, M. F., Fulgham, S. R., Brophy, P., Galang, A., Brune, W. H., Jathar, S. H., and Farmer, D. K.:
282 Primary and Secondary Sources of Gas-Phase Organic Acids from Diesel Exhaust, *Environ. Sci. Technol.*, 51, 10872-10880,
283 10.1021/acs.est.7b01169, 2017.

284 Fuzzi, S., Baltensperger, U., Carslaw, K., Decesari, S., Denier van der Gon, H., Facchini, M. C., Fowler, D., Koren, I.,
285 Langford, B., Lohmann, U., Nemitz, E., Pandis, S., Riipinen, I., Rudich, Y., Schaap, M., Slowik, J. G., Spracklen, D. V.,
286 Vignati, E., Wild, M., Williams, M., and Gilardoni, S.: Particulate matter, air quality and climate: lessons learned and future
287 needs, *Atmos. Chem. Phys.*, 15, 8217-8299, 10.5194/acp-15-8217-2015, 2015.

288 Gentner, D. R., Jathar, S. H., Gordon, T. D., Bahreini, R., Day, D. A., El Haddad, I., Hayes, P. L., Pieber, S. M., Platt,
289 S. M., and de Gouw, J. A.: A review of urban secondary organic aerosol formation from gasoline and diesel motor vehicle
290 emissions, *Environ. Sci. Technol.*, 2016.

291 Gordon, T. D., Nguyen, N. T., Presto, A. A., Lipsky, E. M., Maldonado, S., Maricq, M., and Robinson, A. L.:
292 Secondary organic aerosol production from diesel vehicle exhaust: impact of aftertreatment, fuel chemistry and driving cycle,
293 *Atmospheric Chemistry & Physics*, 14, 4643-4659, doi:10.5194/acp-14-4643-2014, 2014.

294 Hayes, P., Carlton, A., Baker, K., Ahmadov, R., Washenfelder, R., Alvarez, S., Rappenglück, B., Gilman, J., Kuster,
295 W., and de Gouw, J.: Modeling the formation and aging of secondary organic aerosols in Los Angeles during CalNex 2010,
296 *Atmospheric Chemistry and Physics*, 15, 5773-5801, 2015.

297 Hildebrandt, L., Donahue, N., and Pandis, S.: High formation of secondary organic aerosol from the photo-oxidation

298 of toluene, *Atmospheric Chemistry and Physics*, 9, 2973-2986, doi:10.5194/acp-9-2973-2009, 2009.

299 Hodzic, A., Jimenez, J., Madronich, S., Canagaratna, M., DeCarlo, P., Kleinman, L., and Fast, J.: Modeling organic
300 aerosols in a megacity: potential contribution of semi-volatile and intermediate volatility primary organic compounds to
301 secondary organic aerosol formation, *Atmospheric Chemistry and Physics*, 10, 5491-5514, doi:10.5194/acp-10-5491-2010,
302 2010.

303 Huffman, J., Docherty, K., Mohr, C., Cubison, M., Ulbrich, I., Ziemann, P., Onasch, T., and Jimenez, J.: Chemically-
304 resolved volatility measurements of organic aerosol from different sources, *Environ. Sci. Technol.*, 43, 5351-5357, 2009.

305 Jathar, S., Farina, S., Robinson, A., and Adams, P.: The influence of semi-volatile and reactive primary emissions on
306 the abundance and properties of global organic aerosol, *Atmospheric Chemistry and Physics*, 11, 7727-7746, doi:10.5194/acp-
307 11-7727-2011 2011.

308 Jathar, S. H., Donahue, N. M., Adams, P. J., and Robinson, A. L.: Testing secondary organic aerosol models using
309 smog chamber data for complex precursor mixtures: influence of precursor volatility and molecular structure, *Atmospheric*
310 *Chemistry and Physics*, 14, 5771-5780, 2014a.

311 Jathar, S. H., Gordon, T. D., Hennigan, C. J., Pye, H. O. T., Pouliot, G. A., Adams, P. J., Donahue, N. M., and
312 Robinson, A. L.: Unspeciated organic emissions from combustion sources and their influence on the secondary organic aerosol
313 budget in the United States, *Proceedings of the National Academy of Sciences*, 111, 10473-10478, 2014b.

314 Jathar, S. H., Cappa, C. D., Wexler, A. S., Seinfeld, J. H., and Kleeman, M. J.: Multi-generational oxidation model to
315 simulate secondary organic aerosol in a 3-D air quality model, *Geosci. Model Dev.*, 8, 2553-2567, 10.5194/gmd-8-2553-2015,
316 2015.

317 Jathar, S. H., Cappa, C. D., Wexler, A. S., Seinfeld, J. H., and Kleeman, M. J.: Simulating secondary organic aerosol
318 in a regional air quality model using the statistical oxidation model – Part 1: Assessing the influence of constrained multi-
319 generational ageing, *Atmospheric Chemistry & Physics*, 16, 2309-2322, 2016.

320 Jathar, S. H., Friedman, B., Galang, A. A., Link, M. F., Brophy, P., Volckens, J., Eluri, S., and Farmer, D. K.: Linking
321 Load, Fuel and Emission Controls to Photochemical Production of Secondary Organic Aerosol from a Diesel Engine, *Environ.*
322 *Sci. Technol.*, 2017a.

323 Jathar, S. H., Woody, M., Pye, H. O., Baker, K. R., and Robinson, A. L.: Chemical transport model simulations of
324 organic aerosol in southern California: model evaluation and gasoline and diesel source contributions, *Atmospheric Chemistry*
325 *and Physics*, 17, 4305-4318, 2017b.

326 Karnezi, E., Riipinen, I., and Pandis, S.: Measuring the atmospheric organic aerosol volatility distribution: a
327 theoretical analysis, *Atmospheric Measurement Techniques*, 7, 2953-2965, 2014.

328 Konovalov, I. B., Beekmann, M., Berezin, E. V., Petetin, H., Mielonen, T., Kuznetsova, I. N., and Andreae, M. O.:
329 The role of semi-volatile organic compounds in the mesoscale evolution of biomass burning aerosol: a modelling case study of
330 the 2010 mega-fire event in Russia, *Atmospheric Chemistry and Physics Discussions*, 15, 9107-9172, 2015.

331 Krechmer, J. E., Pagonis, D., Ziemann, P. J., and Jimenez, J. L. L.: Quantification of gas-wall partitioning in Teflon
332 environmental chambers using rapid bursts of low-volatility oxidized species generated in-situ, *Environ. Sci. Technol.*, 2016.

333 Krechmer, J. E., Day, D. A., Ziemann, P. J., and Jimenez, J. L. L.: Direct measurements of gas/particle partitioning and
334 mass accommodation coefficients in environmental chambers, *Environ. Sci. Technol.*, 51, 11867-11875, 2017.

335 Kroll, J. H., Smith, J. D., Che, D. L., Kessler, S. H., Worsnop, D. R., and Wilson, K. R.: Measurement of
336 fragmentation and functionalization pathways in the heterogeneous oxidation of oxidized organic aerosol, *Physical Chemistry*

337 Chemical Physics, 11, 8005-8014, 2009.

338 Lambe, A., Chhabra, P., Onasch, T., Brune, W., Hunter, J., Kroll, J., Cummings, M., Brogan, J., Parmar, Y., and
339 Worsnop, D.: Effect of oxidant concentration, exposure time, and seed particles on secondary organic aerosol chemical
340 composition and yield, *Atmospheric Chemistry and Physics*, 15, 3063-3075, 2015.

341 Lambe, A. T., Ahern, A. T., Williams, L. R., Slowik, J. G., Wong, J. P. S., Abbatt, J. P. D., Brune, W. H., Ng, N. L.,
342 Wright, J. P., and Croasdale, D. R.: Characterization of aerosol photooxidation flow reactors: heterogeneous oxidation,
343 secondary organic aerosol formation and cloud condensation nuclei activity measurements, *Atmospheric Measurement
344 Techniques*, 4, 445-461, 2011.

345 Lambe, A. T., Onasch, T. B., Croasdale, D. R., Wright, J. P., Martin, A. T., Franklin, J. P., Massoli, P., Kroll, J. H.,
346 Canagaratna, M. R., and Brune, W. H.: Transitions from functionalization to fragmentation reactions of laboratory secondary
347 organic aerosol (SOA) generated from the OH oxidation of alkane precursors, *Environ. Sci. Technol.*, 46, 5430-5437, 2012.

348 Lee, B.-H., Pierce, J. R., Engelhart, G. J., and Pandis, S. N.: Volatility of secondary organic aerosol from the
349 ozonolysis of monoterpenes, *Atmospheric environment*, 45, 2443-2452, 2011.

350 Lim, Y. B., and Ziemann, P. J.: Effects of molecular structure on aerosol yields from OH radical-initiated reactions of
351 linear, branched, and cyclic alkanes in the presence of NO_x, *Environ. Sci. Technol.*, 43, 2328-2334, 2009.

352 Link, M., Friedman, B., Fulgham, R., Brophy, P., Galang, A., Jathar, S., Veres, P., Roberts, J., and Farmer, D.:
353 Photochemical processing of diesel fuel emissions as a large secondary source of isocyanic acid (HNCO), *Geophysical
354 Research Letters*, 43, 4033-4041, 2016.

355 May, A. A., Levin, E. J. T., Hennigan, C. J., Riipinen, I., Lee, T., Collett, J. L., Jimenez, J. L., Kreidenweis, S. M., and
356 Robinson, A. L.: Gas-particle partitioning of primary organic aerosol emissions: 3. Biomass burning, *Journal of Geophysical
357 Research: Atmospheres*, 118, 2013JD020286, 10.1002/jgrd.50828, 2013a.

358 May, A. A., Presto, A. A., Hennigan, C. J., Nguyen, N. T., Gordon, T. D., and Robinson, A. L.: Gas-particle
359 partitioning of primary organic aerosol emissions: (2) Diesel vehicles, *Environ. Sci. Technol.*, 47, 8288-8296, 2013b.

360 May, A. A., Presto, A. A., Hennigan, C. J., Nguyen, N. T., Gordon, T. D., and Robinson, A. L.: Gas-particle
361 partitioning of primary organic aerosol emissions: (1) gasoline vehicle exhaust, *Atmospheric Environment*, 77, 128-139,
362 2013c.

363 Murphy, B., and Pandis, S.: Simulating the formation of semivolatile primary and secondary organic aerosol in a
364 regional chemical transport model., *Environ. Sci. Technol.*, 43, 4722-4728, doi:10.1021/es803168a, 2009.

365 Ng, N., Kroll, J., Chan, A., Chhabra, P., Flagan, R., and Seinfeld, J.: Secondary organic aerosol formation from m-
366 xylene, toluene, and benzene, *Atmos. Chem. Phys.*, 7, 3909-3922, doi:10.5194/acp-7-3909-2007, 2007.

367 Odum, J. R., Hoffmann, T., Bowman, F., Collins, D., Flagan, R. C., and Seinfeld, J. H.: Gas/particle partitioning and
368 secondary organic aerosol yields, *Environ. Sci. Technol.*, 30, 2580-2585, 1996.

369 Ortega, A. M., Hayes, P. L., Peng, Z., Palm, B. B., Hu, W., Day, D. A., Li, R., Cubison, M. J., Brune, W. H., and
370 Graus, M.: Real-time measurements of secondary organic aerosol formation and aging from ambient air in an oxidation flow
371 reactor in the Los Angeles area, *Atmospheric Chemistry and Physics*, 16, 7411-7433, 2016.

372 Pachauri, R. K., Allen, M. R., Barros, V. R., Broome, J., Cramer, W., Christ, R., Church, J. A., Clarke, L., Dahe, Q.,
373 Dasgupta, P., Dubash, N. K., Edenhofer, O., Elgizouli, I., Field, C. B., Forster, P., Friedlingstein, P., Fuglestvedt, J., Gomez-
374 Echeverri, L., Hallegatte, S., Hegerl, G., Howden, M., Jiang, K., Jimenez Cisneroz, B., Kattsov, V., Lee, H., Mach, K. J.,
375 Marotzke, J., Mastrandrea, M. D., Meyer, L., Minx, J., Mulugetta, Y., O'Brien, K., Oppenheimer, M., Pereira, J. J., Pichs-

376 Madruga, R., Plattner, G. K., Pörtner, H.-O., Power, S. B., Preston, B., Ravindranath, N. H., Reisinger, A., Riahi, K.,
377 Rusticucci, M., Scholes, R., Seyboth, K., Sokona, Y., Stavins, R., Stocker, T. F., Tschakert, P., van Vuuren, D., and van
378 Ypserle, J. P.: Climate Change 2014: Synthesis Report. Contribution of Working Groups I, II and III to the Fifth Assessment
379 Report of the Intergovernmental Panel on Climate Change, edited by: Pachauri, R. K., and Meyer, L., IPCC, Geneva,
380 Switzerland, 151 pp., 2014.

381 Palm, B. B., Campuzano-Jost, P., Ortega, A. M., Day, D. A., Kaser, L., Jud, W., Karl, T., Hansel, A., Hunter, J. F.,
382 and Cross, E. S.: In situ secondary organic aerosol formation from ambient pine forest air using an oxidation flow reactor,
383 *Atmospheric Chemistry and Physics*, 16, 2943-2970, 2016.

384 Pankow, J. F.: An absorption model of gas/particle partitioning of organic compounds in the atmosphere, *Atmospheric*
385 *Environment*, 28, 185-188, 1994.

386 Pankow, J. F., and Barsanti, K. C.: The carbon number-polarity grid: A means to manage the complexity of the mix of
387 organic compounds when modeling atmospheric organic particulate matter, *Atmospheric Environment*, 43, 2829-2835, 2009.

388 Peng, Z., Day, D., Stark, H., Li, R., Lee-Taylor, J., Palm, B., Brune, W., and Jimenez, J.: HOx radical chemistry in
389 oxidation flow reactors with low-pressure mercury lamps systematically examined by modeling, *Atmospheric Measurement*
390 *Techniques*, 8, 4863-4890, 2015.

391 Presto, A. A., Miracolo, M. A., Donahue, N. M., and Robinson, A. L.: Secondary organic aerosol formation from
392 high-NO_x photo-oxidation of low volatility precursors: n-alkanes, *Environ. Sci. Technol.*, 44, 2029-2034, 2010.

393 Presto, A. A., Nguyen, N. T., Ranjan, M., Reeder, A. J., Lipsky, E. M., Hennigan, C. J., Miracolo, M. A., Riemer, D.
394 D., and Robinson, A. L.: Fine particle and organic vapor emissions from staged tests of an in-use aircraft engine, *Atmospheric*
395 *Environment*, 45, 3603-3612, 2011.

396 Pye, H., and Seinfeld, J.: A global perspective on aerosol from low-volatility organic compounds, *Atmos. Chem.*
397 *Phys*, 10, 4377-4401, doi:10.5194/acp-10-4377-2010, 2010.

398 Robinson, A. L., Donahue, N. M., Shrivastava, M. K., Weitkamp, E. A., Sage, A. M., Grieshop, A. P., Lane, T. E.,
399 Pierce, J. R., and Pandis, S. N.: Rethinking organic aerosols: Semivolatile emissions and photochemical aging, *Science*, 315,
400 1259-1262, 2007.

401 Saleh, R., Donahue, N. M., and Robinson, A. L.: Time scales for gas-particle partitioning equilibration of secondary
402 organic aerosol formed from alpha-pinene ozonolysis, *Environ. Sci. Technol.*, 47, 5588-5594, 2013.

403 Seinfeld, J. H., and Pandis, S. N.: *Atmospheric Chemistry and Physics*, John Wiley and Sons, New York, 2006.

404 Simonen, P., Saukko, E., Karjalainen, P., Timonen, H., Bloss, M., Aakko-Saksa, P., Rönkkö, T., Keskinen, J., and Dal
405 Maso, M.: A new oxidation flow reactor for measuring secondary aerosol formation of rapidly changing emission sources,
406 *Atmospheric Measurement Techniques*, 10, 1519, 2017.

407 Song, C., Na, K., Warren, B., Malloy, Q., and Cocker III, D. R.: Secondary organic aerosol formation from the
408 photooxidation of p- and o-xylene, *Environ. Sci. Technol.*, 41, 7403-7408, 2007.

409 Tkacik, D. S., Presto, A. A., Donahue, N. M., and Robinson, A. L.: Secondary organic aerosol formation from
410 intermediate-volatility organic compounds: cyclic, linear, and branched alkanes, *Environ. Sci. Technol.*, 46, 8773-8781, doi:
411 10.1021/es301112c, 2012.

412 Tkacik, D. S., Lambe, A. T., Jathar, S., Li, X., Presto, A. A., Zhao, Y., Blake, D., Meinardi, S., Jayne, J. T., Croteau,
413 P. L., and Robinson, A. L.: Secondary Organic Aerosol Formation from in-Use Motor Vehicle Emissions Using a Potential
414 Aerosol Mass Reactor, *Environ. Sci. Technol.*, 48, 11235-11242, 10.1021/es502239v, 2014.

415 Tsimpidi, A., Karydis, V., Zavala, M., Lei, W., Molina, L., Ulbrich, I., Jimenez, J., and Pandis, S.: Evaluation of the
416 volatility basis-set approach for the simulation of organic aerosol formation in the Mexico City metropolitan area, *Atmos.*
417 *Chem. Phys.*, 10, 525-546, doi:10.5194/acp-10-525-2010, 2009.

418 Zhang, X., Cappa, C. D., Jathar, S. H., McVay, R. C., Ensberg, J. J., Kleeman, M. J., and Seinfeld, J. H.: Influence of
419 vapor wall loss in laboratory chambers on yields of secondary organic aerosol, *Proceedings of the National Academy of*
420 *Sciences*, 111, 5802-5807, 2014.

421 Zhao, Y., Nguyen, N. T., Presto, A. A., Hennigan, C. J., May, A. A., and Robinson, A. L.: Intermediate volatility
422 organic compound emissions from on-road diesel vehicles: chemical composition, emission factors, and estimated secondary
423 organic aerosol production, *Environ. Sci. Technol.*, 49, 11516-11526, 2015.

424

426

427 *Table 1: Primary emissions of THC and POA, maximum photochemical production of SOA, maximum O:C of the OA, maximum OH exposure,*
 428 *and size distribution data from Jathar et al. (2017a).*

Deleted: .

<i>Load-Fuel- Aftertreatment Experiment</i>	<i>Date</i>	<i>THC ($\mu\text{g m}^{-3}$)</i>	<i>CO (ppbv)</i>	<i>NO (ppbv)</i>	<i>NO₂ (ppbv)</i>	<i>POA ($\mu\text{g m}^{-3}$)</i>	<i>SOA% ($\mu\text{g m}^{-3}$)</i>	<i>O: C%</i>	<i>OH Exposure% (molec.-hr cm⁻³)</i>	<i>Number Mean Dia.* (nm)</i>	<i>Number Conc.* ($\# \text{ cm}^{-3}$)</i>
Idle-Diesel-None	June 3	1519	2746	960	318	38±15	209±66	0.23±0.01	2.1×10 ⁷		8.0×10 ⁵
	June 5	1810	5809	878	502	35±11	875±288	0.46±0.07	6.67×10 ⁷	46	6.5×10 ⁵
	June 12	2554	9664	1870	1103	85±17	877±277	0.57±0.09	3.61×10 ⁷		3.4×10 ⁵
Idle-Biodiesel-None	June 4	1118	4270	867	344	22±12	999±316	0.52±0.07	9.17×10 ⁷	46 [@]	7.3×10 ^{5@}
	June 8	2160	8169	1578	811	69±20	1415±468	0.36±0.03	4.72×10 ⁷		4.1×10 ^{5@}
Load-Diesel-None	June 3	959	1558	4999	379	19±11	181±58	0.37±0.01	3.6×10 ⁷	190	5.3×10 ⁵
	June 5	711	1400	6690	34	37±13	253±100	0.32±0.04	2.61×10 ⁷		4.4×10 ⁵
Load- Biodiesel-None	June 4	1634	1410	6364	30	29±18	645±204	0.38±0.05	2.78×10 ⁷	190 [@]	5.0×10 ^{5@}
	June 8	518	2051	10813	496	46±22	284±106	0.30±0.04	1.42×10 ⁷		3.3×10 ^{5@}
Idle-Diesel-DPF+DOC	June 9	2135	7473	2383	23	1.5±0.6	1040±335	0.37±0.02	5×10 ⁷	52	910
Load-Diesel-DPF+DOC	June 9	303	85	6157	4483	1.6±3.6	146±48	0.29±0.01	1.31×10 ⁷	57	968
Idle-Biodiesel- DPF+DOC	June 10	1773	7452	2213	182	2.6±1	787±250	0.44±0.04	5.28×10 ⁷	52 [@]	910 [@]
Load-Biodiesel- DPF+DOC	June 10	261	58	5475	4525	2±0.14	107±9	0.29±0.01	1.39×10 ⁷	57 [@]	968 [@]

429 DPF=diesel particulate filter, DOC=diesel oxidation catalyst

430 %maximum values measured in each experiment

431 * values measured at no OH exposure

432 @No data, assumed to be similar to the equivalent diesel experiment for the model

436

Table 2: SOA precursors and mass yields used in the VBS model for high NO_x conditions.

Species	log ₁₀ C*					Reference
	0.1	1	10	100	1000	
toluene	0.0000	0.0100	0.2400	0.4500	0.7000	Hildebrandt et al. (2009)
benzene	0.0392	0.0315	0.0000	0.8230	0.0957	Ng et al. (2007) [#]
m-xylene	0.0032	0.0106	0.0633	0.0465	0.0000	Ng et al. (2007) [#]
p-xylene	0.0000	0.0022	0.0764	0.0000	0.0000	Song et al. (2007) [#]
o-xylene	0.0000	0.0132	0.1140	0.0000	0.0000	Song et al. (2007) [#]
naphthalene	0.0000	0.1660	0.0000	0.5400	0.8130	Chan et al. (2009) [#]
1-methylnaphthalene	0.0000	0.0170	0.4860	0.0000	0.0000	Chan et al. (2009) [#]
2-methylnaphthalene	0.0000	0.0531	0.5040	0.0000	0.0000	Chan et al. (2009) [#]
1,2-dimethylnaphthalene	0.0000	0.3100	0.0000	0.0000	0.0000	Chan et al. (2009) [#]
1-methyl-3-n-propylbenzene	0.0000	0.0000	0.0405	0.0694	0.1140	Odum et al. (1996) [#]
n-decane	0.0000	0.0000	0.0110	0.1280	0.2420	Presto et al. (2010) ^{&}
n-undecane	0.0000	0.0040	0.0720	0.1760	0.1450	Presto et al. (2010) ^{&}
n-dodecane	0.0000	0.0140	0.1100	0.1600	0.0000	Presto et al. (2010) ^{&}
n-tridecane	0.0140	0.0590	0.0940	0.0710	0.0000	Presto et al. (2010) ^{&}
n-tetradecane	0.0940	0.3000	0.3500	0.0000	0.0000	Presto et al. (2010) ^{&}
n-pentadecane	0.0440	0.0710	0.4100	0.3000	0.0000	Presto et al. (2010) ^{&}
n-hexadecane	0.0530	0.0830	0.4600	0.2500	0.0000	Presto et al. (2010) ^{&}
n-heptadecane	0.0630	0.0890	0.5500	0.2000	0.0000	Presto et al. (2010) ^{&}
n-octadecane	0.0760	0.3195	0.3750	0.1000	0.0000	Presto et al. (2010) ^{&}
n-nonadecane	0.0890	0.5500	0.2000	0.0000	0.0000	Presto et al. (2010) ^{&}
n-eicosane	0.3195	0.3750	0.1000	0.0000	0.0000	Presto et al. (2010) ^{&}
n-heneicosane	0.5500	0.2000	0.0000	0.0000	0.0000	Presto et al. (2010) ^{&}
n-docosane	0.3750	0.1000	0.0000	0.0000	0.0000	Presto et al. (2010) ^{&}

[&]extrapolated from the Presto et al. (2010) data[#]do not account for vapor wall lossesComment [Office6]: Sailaja: Need to now include both low and high NO_x parameters.

Deleted: -

Deleted: x

Deleted: Hildebrandt et al., 2009

Deleted: Ng et al., 2007

Deleted: Ng et al., 2007[#]

Deleted: Song et al., 2007

Deleted: Song et al., 2007[#]

Deleted: Chan et al., 2009

Deleted: Chan et al., 2009[#]Deleted: Chan et al., 2009[#]Deleted: Chan et al., 2009[#]

Deleted: Odum et al., 1997

Deleted: Presto et al., 2010

Deleted: Presto et al., 2010[&]

Deleted: Presto et al., 2010

Deleted: Presto et al., 2010[&]Deleted: Presto et al., 2010[&]

Deleted: n- tricosane

... [2]

437

438

439

440

Table 3: SOA precursors and mass yields used in the VBS model for low NO_x conditions.

Species	C*					Reference
	0.1	1	10	100	1000	
toluene	0.0000	0.0100	0.2400	0.7000	0.7000	Hildebrandt et al. (2009)
benzene	0.0000	0.0000	0.0000	0.3700	0.0000	Ng et al. (2007) [#]
m-xylene	0.0000	0.0000	0.0000	0.0310	0.0000	Ng et al. (2007) [#]
p-xylene	0.0000	0.0000	0.0000	0.0310	0.0000	Ng et al. (2007) [#]
o-xylene	0.0000	0.0000	0.0000	0.0310	0.0000	Ng et al. (2007) [#]
naphthalene	0.0000	0.1565	0.0000	0.1199	0.2708	Chan et al. (2009) [#]
1-methylnaphthalene	0.0000	0.1565	0.0000	0.1199	0.2708	Chan et al. (2009) [#]
2-methylnaphthalene	0.0000	0.1565	0.0000	0.1199	0.2708	Chan et al. (2009) [#]
n-decane	0.0002	0.0050	0.0013	0.3938	0.0278	Loza et al. (2014) ^{&}
n-undecane	0.0001	0.0070	0.0216	0.3321	0.0000	Loza et al. (2014) ^{&}
n-dodecane	0.0011	0.0080	0.0279	0.3902	0.0003	Loza et al. (2014) ^{&}
n-tridecane	0.0029	0.0064	0.0551	0.3231	0.7090	Loza et al. (2014) ^{&}
n-tetradecane	0.0004	1.2000	0.1777	0.0194	0.0014	Loza et al. (2014) ^{&}
n-pentadecane	0.0032	0.0124	0.0686	0.5050	0.0025	Loza et al. (2014) ^{&}

Deleted: x

Deleted:

Deleted: log₁₀Deleted: Zhang et al. (2014)[#]

Deleted:

Deleted:

Deleted:

Deleted:

Deleted:

Deleted:

Deleted: #

Deleted: #

Deleted: #

Deleted: #

Deleted: #

Deleted: #

methylundecane	2.8200	1.9100	0.9980	0.0010	0.0010	0.0010	Loza et al. (2014)
hexylcyclohexane	5.0000	2.0500	0.8160	0.1810	0.0019	0.0010	Loza et al. (2014)
toluene	1.3100	1.7700	0.1850	0.0010	0.0019	0.8120	Zhang et al. (2014)
benzene	0.0807	1.9700	0.6370	0.0010	0.0021	0.3600	Ng et al. (2007)
m-xylene	1.0800	2.0500	0.1020	0.0010	0.8780	0.0190	Ng et al. (2007)
naphthalene	0.1890	1.8700	0.3520	0.0543	0.5330	0.0609	Chan et al. (2009)

523
524
525
526
527

Table 6: (a) Volatility- and (b) carbon-number resolved distributions used to determine mass concentrations of POC in the VBS and SOM models respectively. The volatility distributions are from (May et al., 2013b)..

C^* ($\mu\text{g m}^{-3}$)	10^{-2}	10^{-1}	10^1	10^2	10^3	10^4	10^5	10^6
f_i	0.03	0.25	0.37	0.23	0.06	0.03	0.01	0.01

528

Carbon No.	<16	16	17	18	19	20	21	22	23	24	25	26	>26
f_i	0.003	0.000	0.058	0.043	0.055	0.094	0.146	0.181	0.178	0.137	0.078	0.026	0.001

529
530
531
532

Table 7: Reaction rate constants (k_{OH}), mass fractions, and VBS and SOM surrogates for SOA precursors in diesel and biodiesel emissions. k_{OH} values are from Atkinson and Arey (2003) when available or the EPI Suite version 4.11 (EPA, 2017).

Species	Carbon Number	k_{OH} ($\text{cm}^3 \text{molecules}^{-1} \text{s}^{-1}$)	Mass Percentage of THC		VBS Surrogate	SOM Surrogate
			Diesel	Biodiesel		
ethylbenzene	8	7.0×10^{-12}	0.2516	0.0826	toluene	toluene
indan	9	1.9×10^{-11}	0.1542	NA	naphthalene	naphthalene
butylbenzene	10	4.5×10^{-12}	0.0081	0.4720	m-xylene	m-xylene
diethylbenzene	10	8.11×10^{-12}	0.0731	NA	m-xylene	m-xylene
isopropyltoluene	10	8.54×10^{-12}	NA	0.3599	toluene	toluene
m-xylene	8	2.31×10^{-11}	0.4951	0.3717	m-xylene	m-xylene
o-xylene	8	1.36×10^{-11}	0.2760	0.3953	o-xylene	m-xylene
p-xylene	8	1.43×10^{-11}	0.0812	NA	p-xylene	m-xylene
n-decane	10	1.1×10^{-11}	0.4302	1.7050	n-decane	n-decane
n-undecane	11	1.23×10^{-11}	0.2110	1.9410	n-undecane	n-dodecane
toluene	7	5.63×10^{-12}	1.1932	1.6401	toluene	toluene
n-tridecane	13	1.68×10^{-11}	NA	0.6136	n-tridecane	n-dodecane
benzaldehyde	7	1.2×10^{-11}	0.5682	NA	benzene	benzene
benzene	6	1.22×10^{-12}	1.6234	1.5988	benzene	benzene
C ₁₀ aromatics	10	2.3×10^{-11}	0.0649	NA	m-xylene	m-xylene
C ₉ aromatics	9	2.31×10^{-11}	0.4058	NA	m-xylene	m-xylene
1,2,3-trimethylbenzene	9	3.27×10^{-11}	0.0974	NA	m-xylene	m-xylene
1,2,4-trimethylbenzene	9	3.25×10^{-11}	0.4302	0.4720	m-xylene	m-xylene

Deleted: 5
Deleted: .
Deleted: 0.144
Deleted: .
Deleted: 0.071
Deleted: .
Deleted: 0.087
Deleted: .
Deleted: 0.065
Deleted: .
Deleted: 0.405
Deleted: .
Deleted: 0.101
Deleted: .
Deleted: 0.308
Deleted: .
Deleted: 0.282
Deleted: .
Deleted: 0.318
Deleted: .
Deleted: 0.338
Deleted: .
Deleted: 0.157
Deleted: 0.046
Deleted: .
Deleted: 0.245
Deleted: .
Deleted: 1.460
Deleted: .
Deleted: 0.120
Deleted: .
Deleted: 1.660
Deleted: .
Deleted: 1.405
Deleted: .
Deleted: 0.680
Deleted: .
Deleted: 0.525
Deleted: .
Deleted: 0.324
Deleted: .
Deleted: 0.925
Deleted: 1.370
Deleted: .
Deleted: 0.037
Deleted: .
Deleted: 0.230
Deleted: .
Deleted: 0.056
Deleted: .
Deleted: 0.245
Deleted: .
Deleted: 0.404

1,2-diethylbenzene	10	8.11×10 ⁻¹²	0.0731	NA	toluene	toluene
1,3,5-trimethylbenzene	9	5.67×10 ⁻¹¹	NA	0.1888	m-xylene	m-xylene
1,2-dimethyl-4-ethylbenzene	10	1.69×10 ⁻¹¹	NA	0.176	m-xylene	m-xylene
1,3-dimethyl-2-ethylbenzene	10	1.76×10 ⁻¹¹	NA	0.3304	m-xylene	m-xylene
1,4-dimethyl-2-ethylbenzene	10	1.69×10 ⁻¹¹	NA	0.4366	m-xylene	m-xylene
1-(1,1-dimethylethyl)-3,5-dimethylbenzene	12	3.01×10 ⁻¹¹	NA	0.3717	m-xylene	m-xylene
1-methyl-2-ethylbenzene	9	7.44×10 ⁻¹²	0.1136	0.3835	toluene	toluene
1-methyl-3-ethylbenzene	9	1.39×10 ⁻¹¹	0.2029	0.7198	toluene	toluene
1-methyl-2-tert-butylbenzene	11	6.74×10 ⁻¹²	NA	0.4307	toluene	toluene
1-tert-butyl-4-ethylbenzene	12	7.42×10 ⁻¹²	NA	0.1947	m-xylene	m-xylene
2-methyl-butylbenzene	11	1.02×10 ⁻¹¹	NA	1.1032	m-xylene	m-xylene
3,3-dimethyloctane	10	7.21×10 ⁻¹²	NA	0.3068	n-decane	methylundecane
3-ethyloctane	10	1.18×10 ⁻¹¹	NA	0.1888	n-decane	methylundecane
3-methylnonane	10	1.14×10 ⁻¹¹	NA	0.2655	n-decane	methylundecane
C ₁₂ branched alkane	12	1.82×10 ⁻¹¹	1.1335	1.1335	n-decane	methylundecane
C ₁₃ branched alkane	13	1.68×10 ⁻¹¹	0.8111	0.8111	n-undecane	methylundecane
C ₁₄ branched alkane	14	1.39×10 ⁻¹¹	0.5257	0.5257	n-dodecane	methylundecane
C ₁₅ branched alkane	15	1.82×10 ⁻¹¹	0.4692	0.4692	n-tridecane	methylundecane
C ₁₆ branched alkane	16	1.96×10 ⁻¹¹	0.4935	0.4935	n-tetradecane	methylundecane
C ₁₇ branched alkane	17	2.1×10 ⁻¹¹	0.2198	0.2198	n-pentadecane	methylundecane
C ₁₈ branched alkane	18	2.24×10 ⁻¹¹	0.2863	0.2863	n-hexadecane	methylundecane
C ₁₉ branched alkane	19	2.38×10 ⁻¹¹	0.1716	0.1716	n-heptadecane	methylundecane
C ₂₀ branched alkane	20	2.52×10 ⁻¹¹	0.0969	0.0969	n-octadecane	methylundecane
C ₂₁ branched alkane	21	2.67×10 ⁻¹¹	0.0639	0.0639	n-nonadecane	methylundecane
C ₂₂ branched alkane	22	2.81×10 ⁻¹¹	0.0604	0.0604	n-eicosane	methylundecane
C ₁₂ cyclic alkane	12	1.82×10 ⁻¹¹	4.3427	4.3427	n-tetradecane	hexylcyclohexane
C ₁₃ cyclic alkane	13	1.68×10 ⁻¹¹	4.4265	4.4265	n-pentadecane	hexylcyclohexane
C ₁₄ cyclic alkane	14	1.39×10 ⁻¹¹	3.1480	3.1480	n-	hexylcyclohexane

4

Deleted: 0.041

Deleted: -

Deleted: 0.162

Deleted: -

Deleted: 0.283

Deleted: -

Deleted: 0.370

Deleted: -

Deleted: 0.318

Deleted: -

Deleted: 0.065

Deleted: -

Deleted: 0.328

Deleted: -

Deleted: 0.116

Deleted: -

Deleted: 0.616

Deleted: -

Deleted: 0.369

Deleted: -

Deleted: 0.166

Deleted: -

Deleted: 0.945

Deleted: -

Deleted: 0.262

Deleted: -

Deleted: 0.162

Deleted: -

Deleted: 0.227

Deleted: 2.268

Deleted: 2.268

Deleted: 1.623

Deleted: 1.623

Deleted: 1.052

Deleted: 1.052

Deleted: 0.939

Deleted: 0.939

Deleted: 0.988

Deleted: 0.988

Deleted: 0.440

Deleted: 0.440

Deleted: 0.573

Deleted: 0.573

Deleted: 0.343

Deleted: 0.343

Deleted: 0.194

Deleted: 0.194

Deleted: 0.128

Deleted: 0.128

Deleted: 0.121

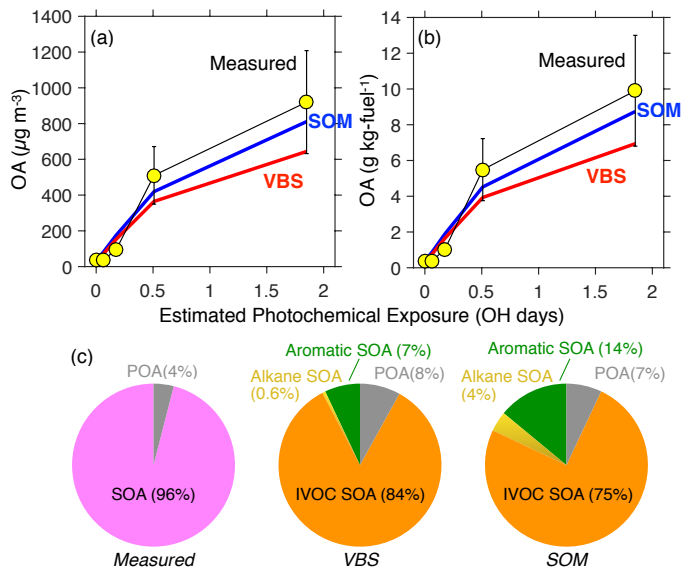
Deleted: 0.121

Deleted: 8.690

Deleted: 8.690

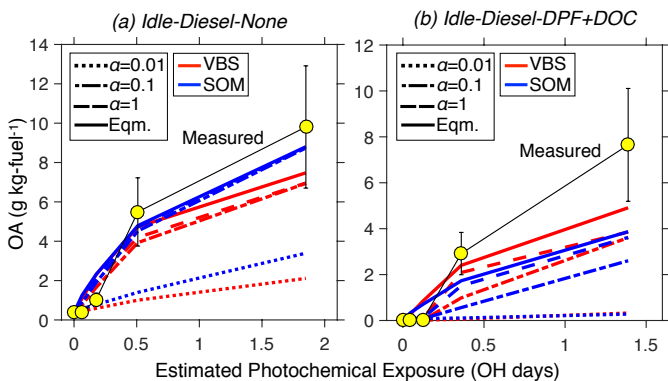
					hexadecane	
C ₁₅ cyclic alkane	15	1.82×10 ⁻¹¹	2.8599	2.8599	<i>n</i> -heptadecane	hexylcyclohexane
C ₁₆ cyclic alkane	16	1.96×10 ⁻¹¹	2.1848	2.1848	<i>n</i> -octadecane	hexylcyclohexane
C ₁₇ cyclic alkane	17	2.1×10 ⁻¹¹	1.8546	1.8546	<i>n</i> -nonadecane	hexylcyclohexane
C ₁₈ cyclic alkane	18	2.24×10 ⁻¹¹	1.6900	1.6900	<i>n</i> -eicosane	hexylcyclohexane
C ₁₉ cyclic alkane	19	2.38×10 ⁻¹¹	1.0570	1.0570	<i>n</i> -heneicosane	hexylcyclohexane
C ₂₀ cyclic alkane	20	2.52×10 ⁻¹¹	0.5900	0.5900	<i>n</i> -docosane	hexylcyclohexane
C ₂₁ cyclic alkane	21	2.67×10 ⁻¹¹	0.3736	0.3736	<i>n</i> -tricosane	hexylcyclohexane
C ₂₂ cyclic alkane	22	2.81×10 ⁻¹¹	0.3141	0.3141	<i>n</i> -tricosane	hexylcyclohexane
dodecane	12	1.82×10 ⁻¹¹	0.5830	0.5830	<i>n</i> -dodecane	<i>n</i> -dodecane
tridecane	13	1.68×10 ⁻¹¹	0.5465	0.5465	<i>n</i> -tridecane	<i>n</i> -dodecane
tetradecane	14	1.39×10 ⁻¹¹	0.3649	0.3649	<i>n</i> -tetradecane	<i>n</i> -dodecane
pentadecane	15	1.82×10 ⁻¹¹	0.3063	0.3063	<i>n</i> -pentadecane	<i>n</i> -dodecane
hexadecane	16	1.96×10 ⁻¹¹	0.2281	0.2281	<i>n</i> -hexadecane	<i>n</i> -dodecane
heptadecane	17	2.1×10 ⁻¹¹	0.1655	0.1655	<i>n</i> -heptadecane	<i>n</i> -dodecane
octadecane	18	2.24×10 ⁻¹¹	0.1481	0.1481	<i>n</i> -octadecane	<i>n</i> -dodecane
nonadecane	19	2.38×10 ⁻¹¹	0.0726	0.0726	<i>n</i> -nonadecane	<i>n</i> -dodecane
eicosane	20	2.52×10 ⁻¹¹	0.0365	0.0365	<i>n</i> -eicosane	<i>n</i> -dodecane
heneicosane	21	2.67×10 ⁻¹¹	0.0222	0.0222	<i>n</i> -heneicosane	<i>n</i> -dodecane
docosane	22	2.81×10 ⁻¹¹	0.0143	0.0143	<i>n</i> -docosane	<i>n</i> -dodecane
pristane	19	2.44×10 ⁻¹¹	0.1434	0.1434	<i>n</i> -nonadecane	methylundecane
phytane	20	2.61×10 ⁻¹¹	0.0799	0.0799	<i>n</i> -eicosane	methylundecane
naphthalene	10	2.3×10 ⁻¹¹	0.1038	0.1038	naphthalene	naphthalene
phenanthrene	14	1.3×10 ⁻¹¹	0.0117	0.0117	naphthalene	naphthalene

Deleted: 5.723
Deleted: 5.723
Deleted: 4.372
Deleted: 4.372
Deleted: 3.711
Deleted: 3.711
Deleted: 3.382
Deleted: 3.382
Deleted: 2.115
Deleted: 2.115
Deleted: 1.181
Deleted: 1.181
Deleted: 0.748
Deleted: 0.748
Deleted: 0.629
Deleted: 0.629
Deleted: 1.167
Deleted: 1.167
Deleted: 1.094
Deleted: 1.094
Deleted: 0.730
Deleted: 0.730
Deleted: 0.613
Deleted: 0.613
Deleted: 0.456
Deleted: 0.456
Deleted: 0.331
Deleted: 0.331
Deleted: 0.296
Deleted: 0.296
Deleted: 0.145
Deleted: 0.145
Deleted: 0.073
Deleted: 0.073
Deleted: 0.044
Deleted: 0.044
Deleted: 0.029
Deleted: 0.029
Deleted: 0.287
Deleted: 0.287
Deleted: 0.160
Deleted: 0.160
Deleted: 0.208
Deleted: 0.208
Deleted: 0.024
Deleted: 0.0235



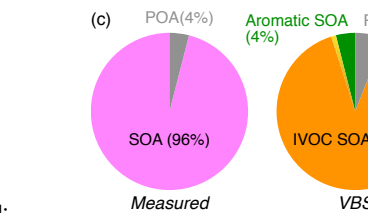
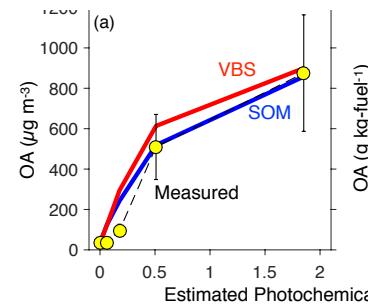
850

851 *Figure 1: VBS and SOM model predictions of OA compared to measurements from the experiment*
 852 *performed on June 5 (Idle-Diesel-None) as a function of photochemical age. Inputs for both models have*
 853 *been specified in the text. Panel (a) has comparisons in $\mu\text{g m}^{-3}$ and panel (b) has comparisons in g kg-*
 854 *fuel⁻¹. Panel (c) shows the modeled and measured OA composition at the highest photochemical exposure.*
 855

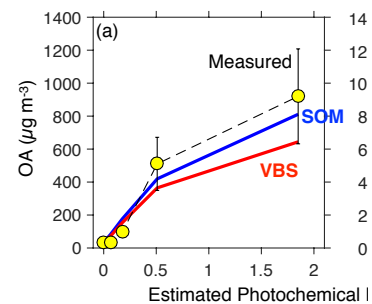


856

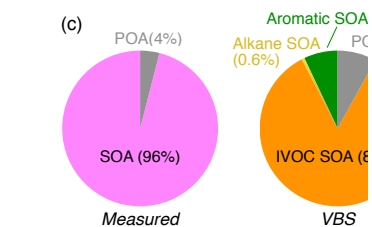
857 *Figure 2: VBS model predictions of OA compared to measurements from the experiment performed on*
 858 *June 5 (Idle-Diesel-None) as a function of photochemical age assuming instantaneous equilibrium*
 859 *partitioning and kinetic gas/particle partitioning run at three accommodation coefficients, $\alpha = 1$ (dash-*
 860 *dot), 0.1 (dash) and 0.01 (solid).*



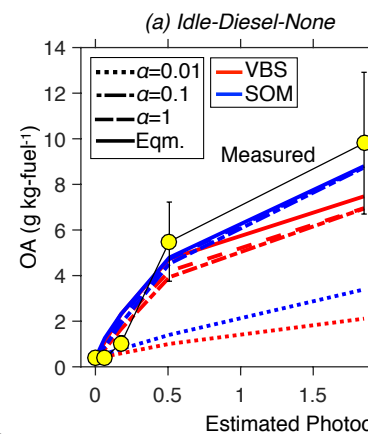
Deleted:



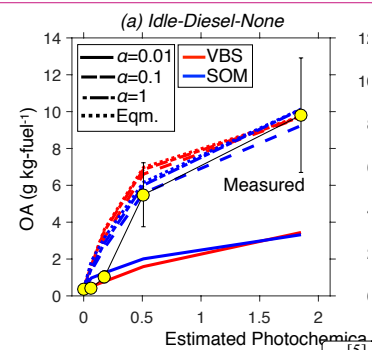
Deleted:



6

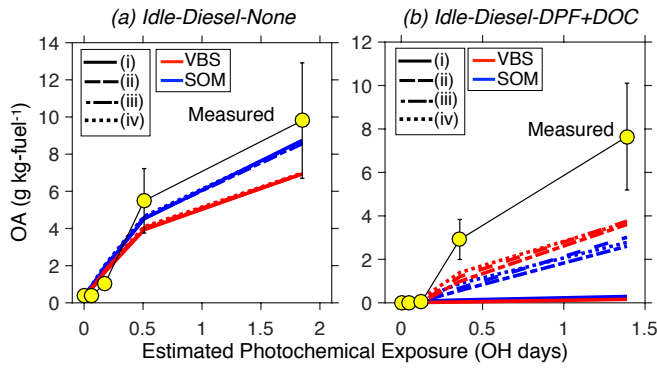


Deleted:



...[5]

873



874
875 *Figure 3: VBS and SOM model predictions of OA compared to measurements from the experiments*
876 *performed on (a) June 5 (Idle-Diesel-None) and (b) June 11 (Idle-Diesel-DPF+DOC) as a function of*
877 *photochemical age for four different particle size distribution inputs: (i) number mean diameter and*
878 *measured number concentration at no OH exposure (solid), (ii) number mean diameter and*
879 *measured number concentration at the given OH exposure (dash), (iii) average of (i) and (ii) (dash-dot), and (iv)*
880 *nucleation of 1 nm particles (dot).*

874

875

876

877

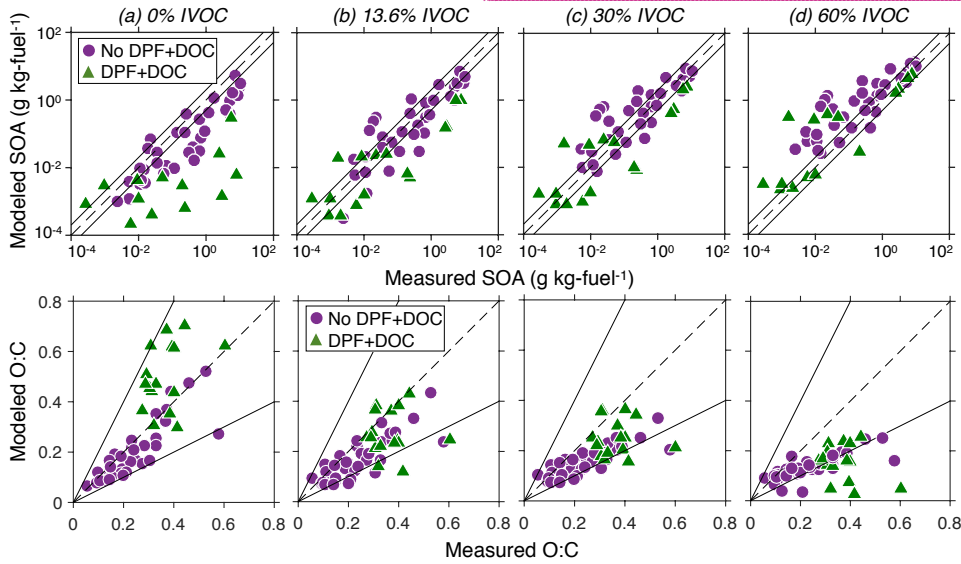
878

879

880

881

882



883
884 *Figure 4: Scatter plot comparing SOM predictions of OA mass and O:C to measurements from all*
885 *experiments at all photochemical ages at four different IVOC mass fractions: (a) 0%, (b) 13.76%, (c)*
886 *30%, and (d) 60%.*

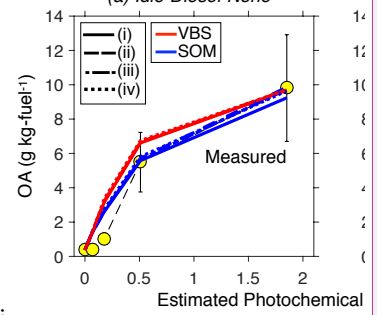
883

884

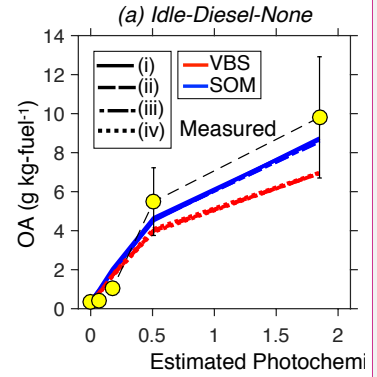
885

886

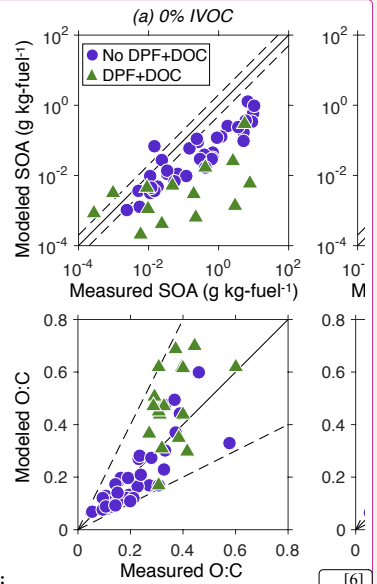
7



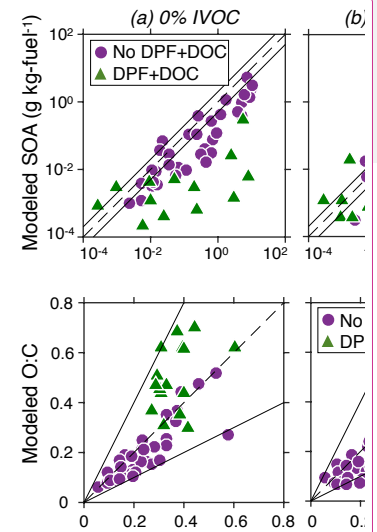
Deleted:



Deleted:



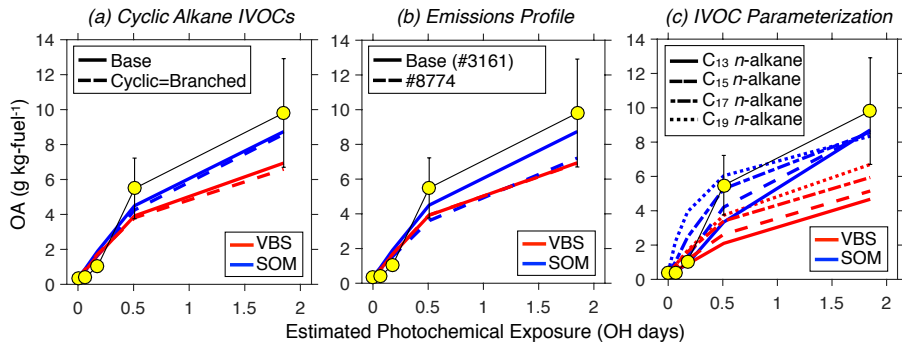
Deleted:



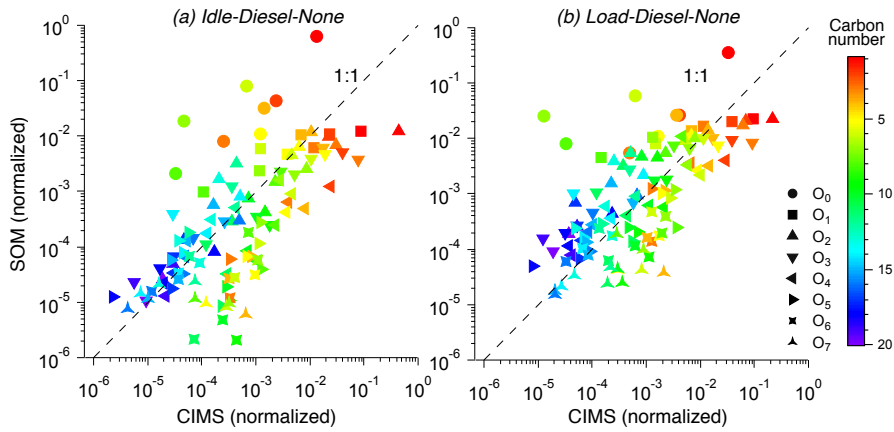
Deleted:

... [7]

904



905
906 *Figure 5: VBS and SOM predictions of OA compared to measurements from the experiment performed on*
907 *June 5 (Idle-Diesel-None) as a function of photochemical age. Panel (a) examines uncertainty in model*
908 *treatment of cyclic alkanes, panel (b) examines uncertainty in the VOC emissions profile, and (c) explores*
909 *suitability of using a single surrogate linear alkane to model SOA formation from all IVOCs.*



911
912 *Figure 6: Normalized gas-phase concentration predictions from the SOM model for the Idle-Diesel-None*
913 *and Load-Diesel-None experiments performed on June 5 and compared to normalized gas-phase*
914 *concentrations measured by the CIMS.*

905

906

907

908

909

910

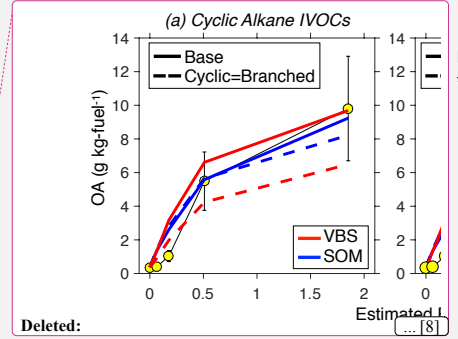
911

912

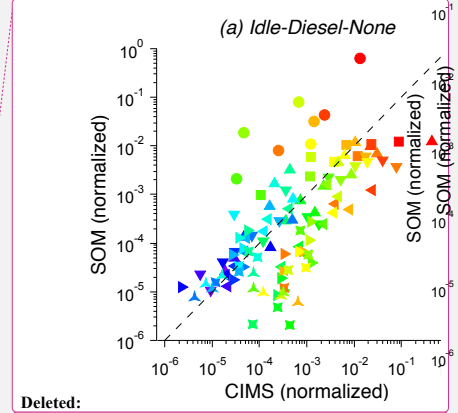
913

914

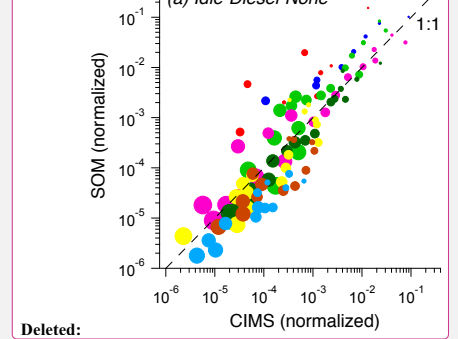
915



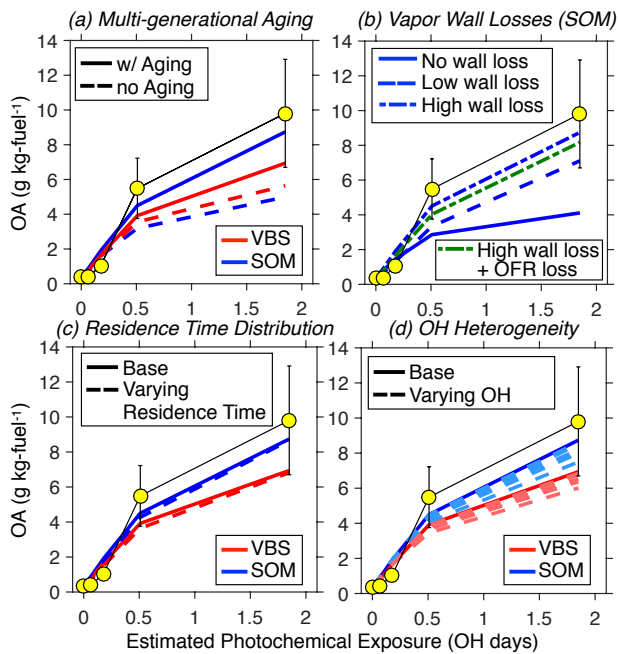
Deleted: ... [8]



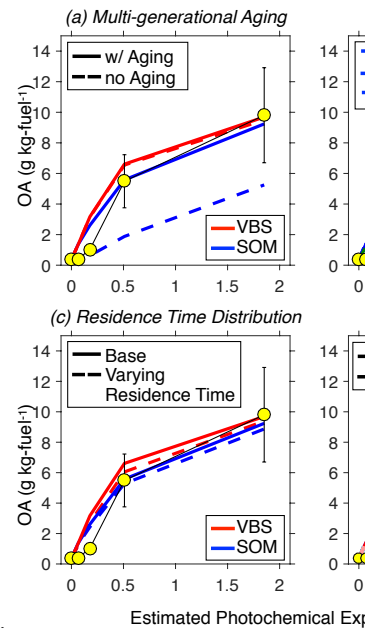
Deleted:



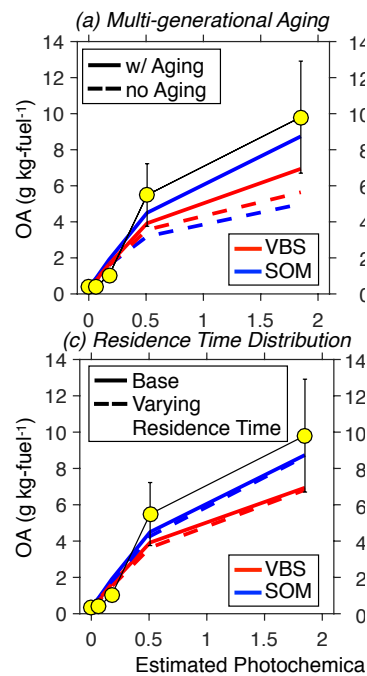
Deleted:



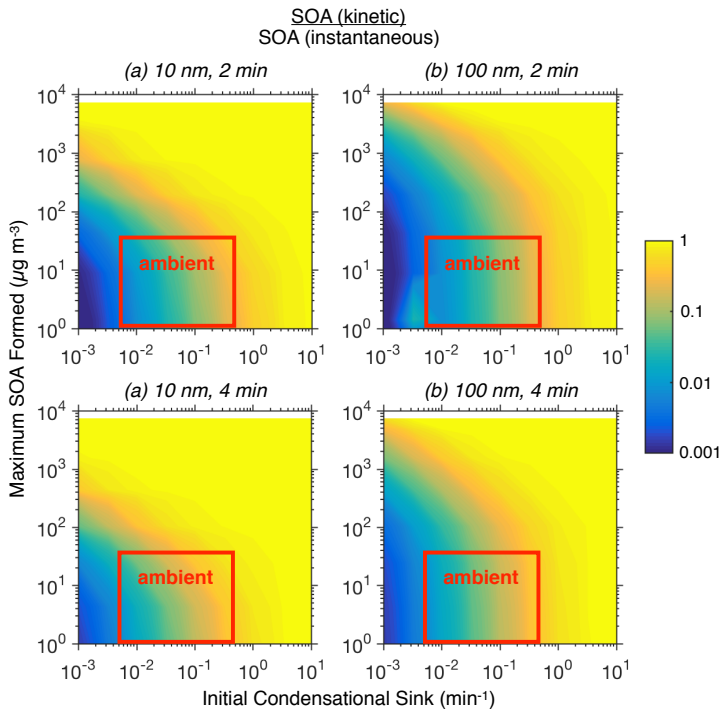
921
 922 Figure 7: VBS and SOM predictions of OA compared to measurements from the experiment performed on
 923 June 5 (Idle-Diesel-None) as a function of photochemical age. Panels (a), (b), (c), and (d) examine the
 924 influence of multi-generational aging, vapor wall losses, residence time distribution, and spatial
 925 heterogeneity in OH concentrations respectively. The dashed lines in panel (d) are deliberately lighter in
 926 color than the solid line to help differentiate the Base result from the sensitivity results.
 927



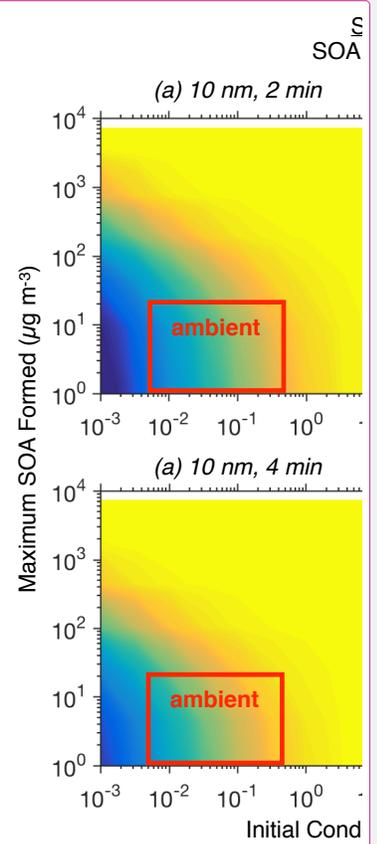
Deleted:



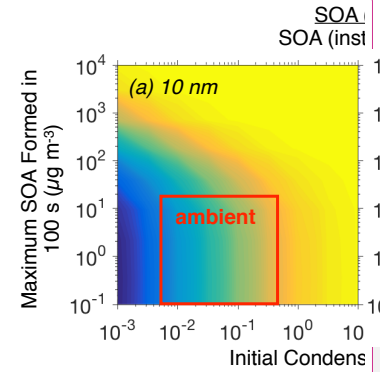
Deleted:



932
 933 *Figure 8: Model predictions of the ratio of SOA produced under kinetic partitioning assumptions to the*
 934 *SOA produced under instantaneous partitioning assumptions as a function of the initial condensational*
 935 *sink and the SOA formed under instantaneous partitioning. Panels (a) and (b) are for calculations*
 936 *performed at two different particles sizes: 10 and 100 nm.*
 937



Deleted:

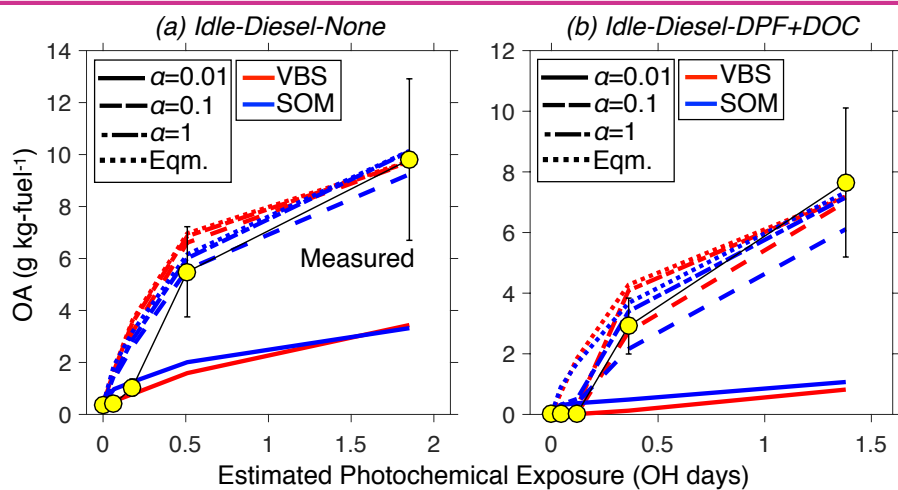
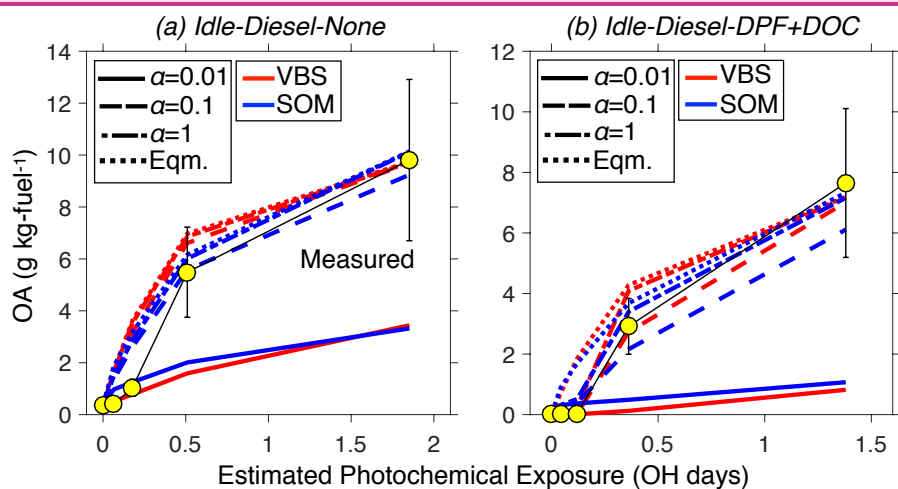


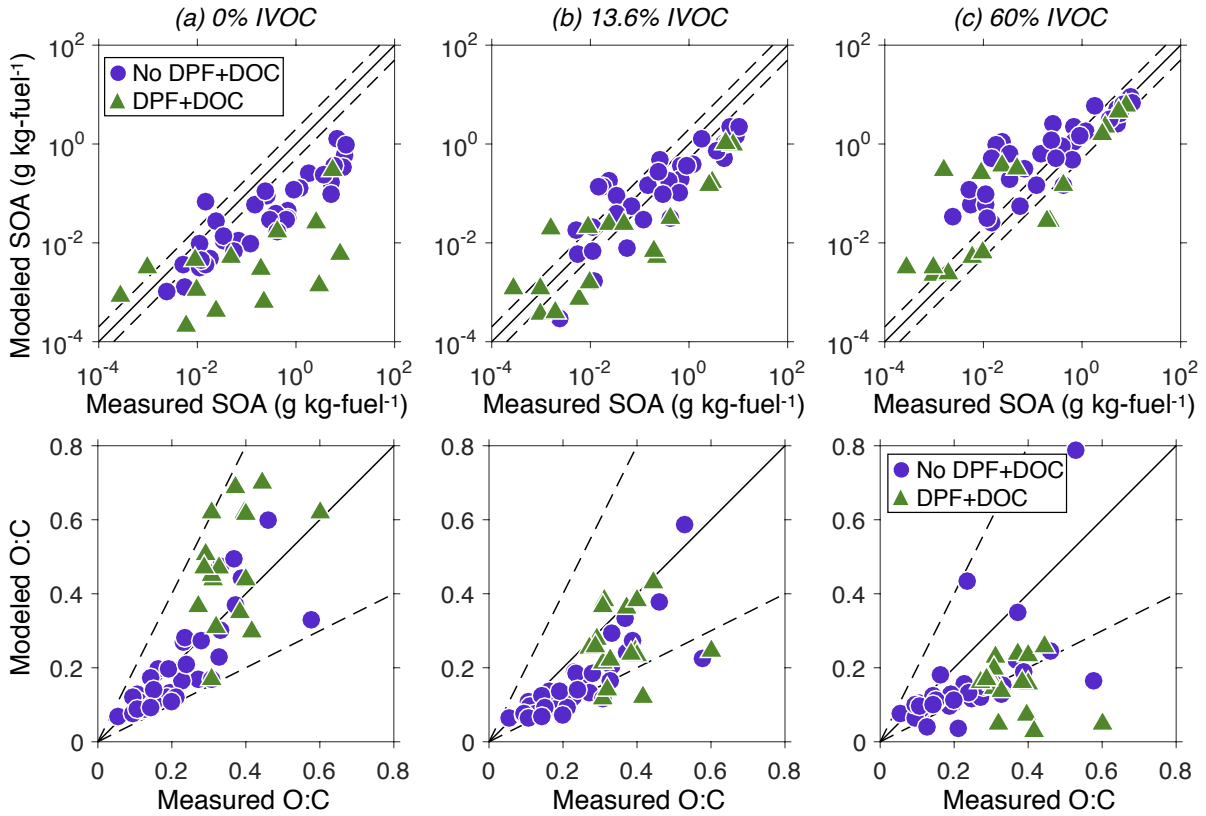
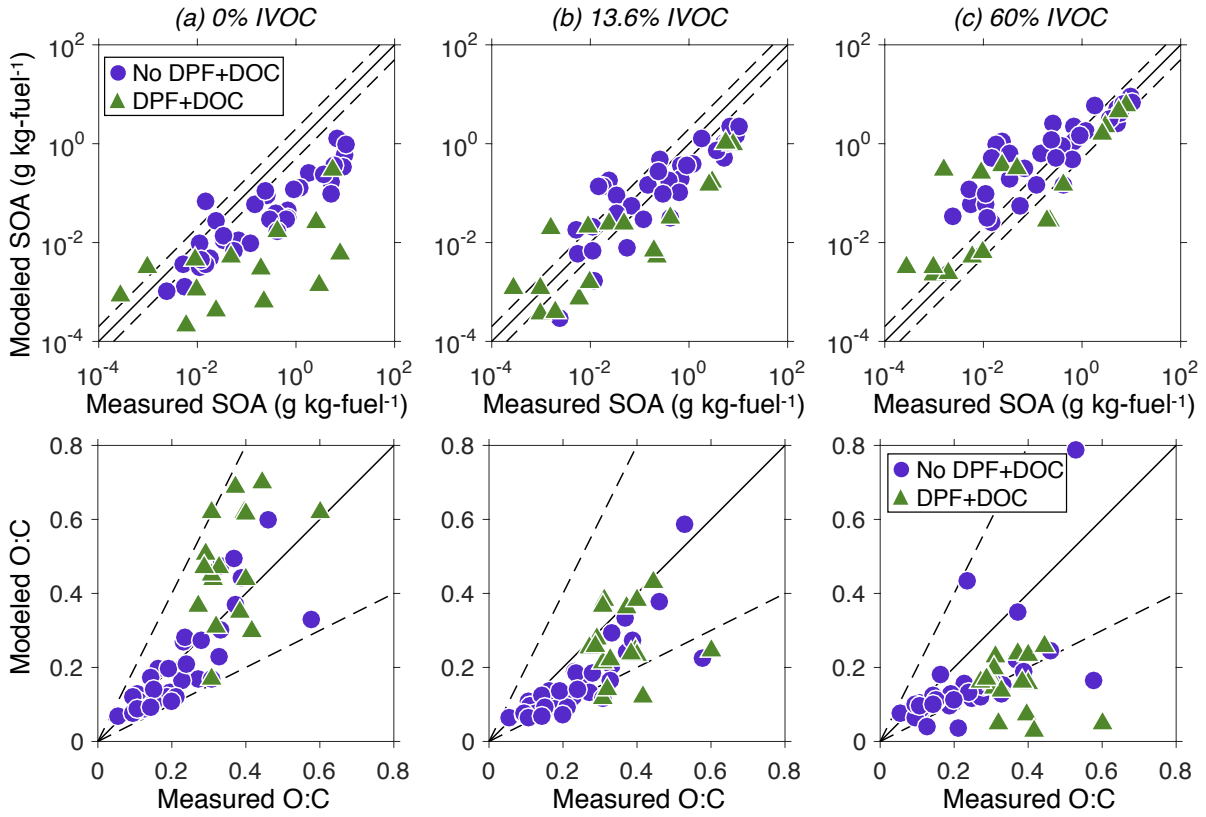
Deleted:

<i>n</i> - tricosane	0.2000	0.000	0.0000	0.0000	0.0000	Presto et al. (2010) ^{&} Presto et al., 2010 ^{&}
----------------------	--------	-------	--------	--------	--------	--

#generated pseudo parameters from SOM

The mass fractions now need to be included for an IVOC mass fraction of 30%.





three

three

three

